Electronic Supplementary Material (ESI) for Nanoscale.
This journal is © The Royal Society of Chemistry 2018

Electronic Supplementary Information (ESI†)

Switchable synchronisation of pirouetting motions in a redox active [3]rotaxane

Hendrik V. Schröder,[a] Amel Mekic,[a] Henrik Hupatz,[a] Sebastian Sobottka,[b] Felix Witte,[a]
Leonhard H. Urner,[a] Marius Gaedke,[a] Kevin Pagel,[ac] Biprajit Sarkar,[b] Beate Paulus[a] and
Christoph A. Schalley[a]*

[a] Institut für Chemie und Biochemie, Freie Universität Berlin
Takustraße 3, 14195 Berlin, Germany.
[b] Institut für Chemie und Biochemie, Freie Universität Berlin
Fabeckstraße 34/36, 14195 Berlin, Germany.
[c] Fritz Haber Institute of the Max Planck Society, Department of Molecular Physics,
Faradayweg 4-6, Berlin, 14195 Berlin, Germany.
*Corresponding author e-mail: c.schalley@fu-berlin.de

Table of contents

1. Experimental and synthetic details

1.1. General methods

All reagents and solvents were obtained from commercial sources and used without further purification. Dry solvents were purchased from Acros Organics. Monomer **exTTF**,[S1] ditosylate **A**,[S2] bis(4-(prop-2-yn-1-yloxy)benzyl)-ammonium hexafluorophosphate,[S3] 4-(prop-2-yn-1-yloxy)benzaldehyde[S4] and 2,6-dimethoxybenzonitrile oxide (**S1**)[S5] were synthesised according to literature procedures. Thin-layer chromatography was performed on silica gel-coated plates with fluorescent indicator F254 (Merck). For column chromatography, silica gel (0.04–0.063 mm, Merck) was used. ^{1}H and ^{13}C NMR experiments were performed on a JEOL ECX 400, JEOL ECP 500 or a Bruker AVANCE 700 MHz instrument. VT NMR experiments were performed on a JEOL ECS 400 MHz spectrometer. Solvent residue signals were used as the internal standard. All shifts are reported in ppm and NMR multiplicities are abbreviated as s (singlet), d (doublet), t (triplet), m (multiplet) and br (broad). Coupling constants *J* are reported in Hertz. Solvents and impurities are marked with an asterisk. High-resolution ESI mass spectra were measured on an Agilent 6210 ESI-TOF instrument (Agilent Technologies). Infrared multiphoton dissociation (IRMPD) experiments were performed on an Ionspec QFT-7 ESI-FTICR mass spectrometer from Varian Inc. equipped with a Micromass/Waters Z-spray electrospray ion source. IR laser pulses of 1000 ms width and 15–25 % laser intensity were applied to initiate fragmentation. HPLC grade solvents were used with a flow rate of 2–4 µL/min. Melting points were determined on a SMP 30 (Stuart) instrument. Melting points are uncorrected. EPR spectra at X-band frequency (ca. 9.5 GHz) were obtained with a Magnettech MS-5000 benchtop EPR spectrometer equipped with a rectangular TE 102 cavity and TC HO4 temperature controller. The measurements were carried out in synthetic quarz glass tubes. Dry and freshly distilled solvents (CH_2Cl_2 and CH_3CN) were used. Sample preparation and measurements were performed under nitrogen. UV/Vis spectra were recorded on a Varian Cary 50 Bio Photospectrometer equipped with a xenon lamp or on an Avantes spectrometer with a light source (AvaLight-DH-S-Bal), a UV/Vis detector (AvaSpec-ULS2048), and a NIR detector (AvaSpec-NIR256-TEC). Solvents with HPLC grade and Suprasil glass cuvettes with a path-length of 1 cm were used. Cyclic voltammetry was performed on an Autolab PGSTAT302N potentiostat using a three-electrode configuration: a freshly polished glassy carbon working electrode, a platinum wire counter electrode and a silver wire pseudoreference electrode. All measurements were conducted twice and with a broad range of different scan rates (25–1000 mV s^{-1}) to ensure electrochemical reversibility of the processes. The decamethylferrocene/ decamethylferrocenium couple was used as internal reference and the determined potentials are given against the ferrocene/ferrocenium (Fc/Fc^+) couple. Dry and argon purged solvents were used.

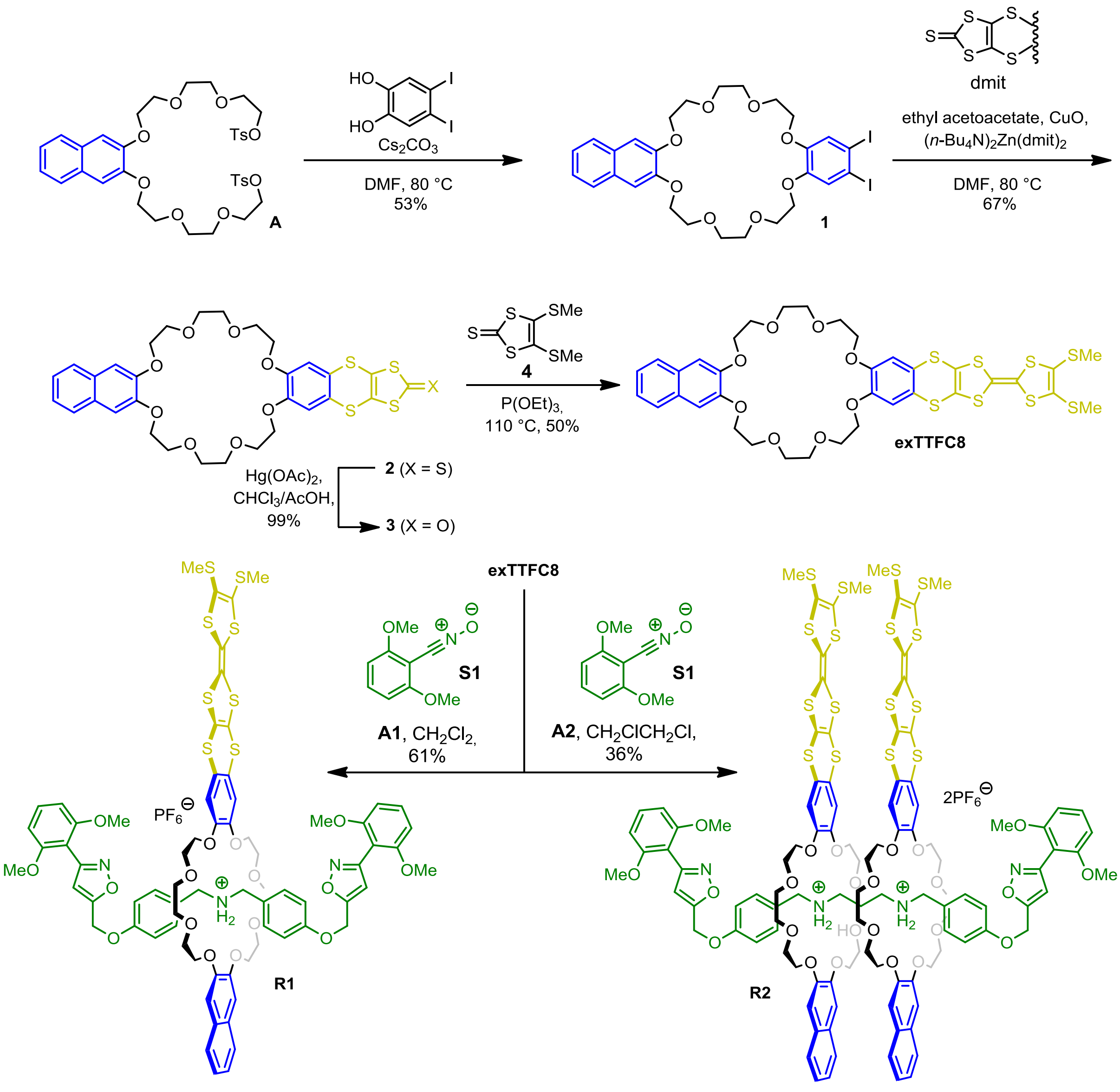

Scheme S1 General synthesis route to macrocycle **exTTFC8** and rotaxanes **R2** and **R3**.

1.2. Synthesis of macrocycle exTTFC8

Diiodide 1

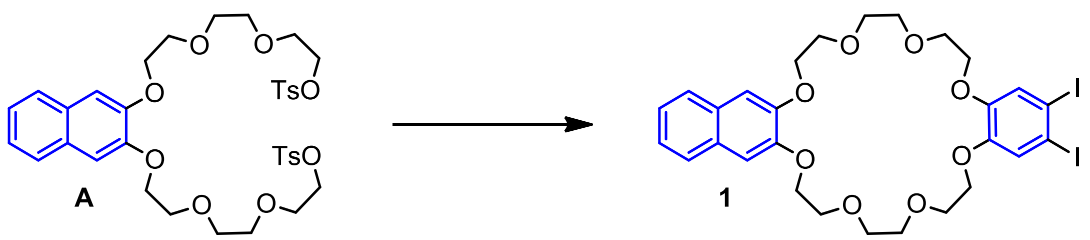

A solution of 4,5-diiodobenzene-1,2-diol (494 mg, 1.36 mmol) in dimethylformamide (DMF, 20 mL) was slowly added to a dispersion of Cs_2CO_3 (1.77 g, 5.44 mmol) in DMF (100 mL) under argon atmosphere. Afterwards, the mixture was heated to 80 °C and a solution of ditosylate **A** (1.000 g, 1.36 mmol) in DMF (150 mL) was added dropwise over 2 h. The reaction was kept at 80 °C for another 2 d, before it was cooled down to room temperature. The solvent was removed *in vacuo* and the residue was dissolved in CH_2Cl_2. After filtering, the filtrate was concentrated *in vacuo* and purified by column chromatography (SiO_2, ethyl acetate/pentane = 3:1). The desired product (540 mg, 0.72 mmol, 53%) was obtained as a white solid. R_f ~ 0.4 in ethyl acetate/pentane = 3:1; m.p. 142 °C; ^{1}H NMR (500 MHz, $CDCl_3$, 298 K): δ = 7.64 (AA'XX' spin system , $^3J_{AA'XX'}$ = 6.1 Hz , 2H, H_{Ar}), 7.32 (AA'XX' spin system, $^3J_{AA'XX'}$ = 6.1 Hz , 2H, H_{Ar}), 7.22 (s, 2H, H_{Ar}), 7.09 (s, 2H, H_{Ar}), 4.27–4.22 (m, 4H, OCH_2), 4.09 – 4.06 (m, 4H, OCH_2), 4.00–3.97 (m, 4H, OCH_2), 3.91–3.85 (m, 8H, OCH_2), 3.83–3.81 (m, 2H, OCH_2) ppm; ^{13}C NMR (126 MHz, $CDCl_3$, 298 K): δ = 149.6, 149.1, 129.4, 126.5, 124.4, 124.1, 108.1, 96.6, 71.6, 71.6, 69.9, 69.8, 69.8, 69.3 ppm; ESI-HRMS: *m/z* calcd for $C_{28}H_{32}O_8I_2$: 788.9818 $[M+K]^+$, found: 788.9850.

Thioketone 2

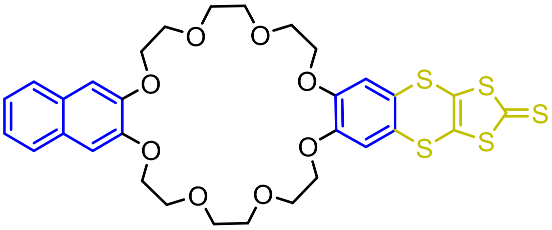

Diiodide **1** (360 mg, 0.48 mmol), $(NEt_4)_2[Zn(dmit)_2]$ (dmit = 1,3-dithiole-2-thione-4,5-dithiolate, 226 mg, 0.24 mmol), Cu_2O (7.2 mg, 0.01 mmol) and ethyl acetoacetate (13 µL, 0.10 mmol) were suspended in DMF (5 mL) and heated to 80 °C overnight. Afterwards, the reaction mixture was cooled down to room temperature and CH_2Cl_2 (20 mL) was added. The resulting mixture was washed with water (4x10 mL) and brine (10 mL) and dried over $MgSO_4$. The crude product was purified by column chromatography (SiO_2, CH_2Cl_2 → CH_2Cl_2/MeOH = 50:1) and the desired product (223 mg, 0.32 mmol, 67%) was obtained as a yellow solid. R_f = 0.4 in CH_2Cl_2/MeOH = 50:1; m.p. >189°C decomposition; ^{1}H NMR (700 MHz, $CDCl_3$. 298 K): δ = 7.64 (AA'XX' spin system, $^3J_{AA'XX'}$ = 6.2 Hz, 2H, HAr), 7.32 (AA'XX' spin system, $^3J_{AA'XX'}$ = 6.2 Hz, 2H, H_{Ar}), 7.09 (s, 2H, H_{Ar}), 6.91 (s, 2H, H_{Ar}), 4.27–4.24 (m, 4H, OCH_2), 4.13–4.10 (m, 4H, OCH_2), 4.01–3.97 (m, 4H, OCH_2), 3.93–3.90 (m, 4H, OCH_2), 3.89–3.86 (m, 4H, OCH_2), 3.84–3.81 (m, 4H, OCH_2) ppm; ^{13}C-NMR (176 MHz, $CDCl_3$, 298 K): δ = 212.8, 149.5, 149.0, 131.9, 129.4, 126.4, 125.7, 124.4, 114.0, 107.9, 71.6, 71.5, 69.9, 69.9, 69.7, 69.3 ppm; ESI-HRMS: *m/z* calcd for $C_{31}H_{32}O_8S_5$: 715.0593 $[M+K]^+$, found: 715.0598.

Ketone 3

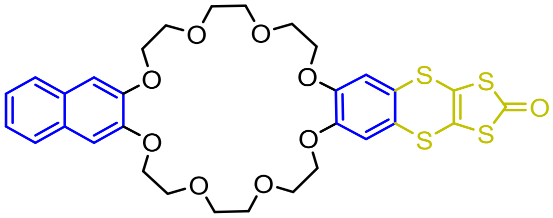

Thione **2** (150 mg, 0.22 mmol) and mercury(II) acetate (210 mg, 0.66 mmol) were dispersed in a mixture of $CHCl_3$ (7 mL) and acetic acid (2 mL) and stirred for 2 days at room temperature. Afterwards, the mixture was filtered through a celite pad, diluted with $CHCl_3$ and washed with saturated aqueous $NaHCO_3$ solution (50 mL) and brine (50 mL). The organic phase was dried over $MgSO_4$ and purified by column chromatography (SiO_2, CH_2Cl_2/Me_2CO = 1:1) to give the desired product (146 mg, 0.22 mmol, 99%) as an off-white solid. R_f = 0.30 in CH_2Cl_2/Me_2CO = 1:1; m. p. 174 °C; ^{1}H NMR (700 MHz, $CDCl_3$, 298 K): δ = 7.64 (m, 2H¸ H_{Ar}), 7.31 (m, 2H¸ H_{Ar}), 7.09 (s, 2H, H_{Ar}), 6.92 (s, 2H, H_{Ar}), 4.27–4.24 (m, 4H, OCH_2), 4.13–4.10 (m, 4H, OCH_2), 4.00–3.97 (m, 4H, OCH_2), 3.92–3.90 (m, 4H, OCH_2), 3.88–3.86 (m, 4H, OCH_2), 3.82 (m, 4H, OCH_2) ppm; ^{13}C NMR (176 MHz, $CDCl_3$, 298 K): δ = 191.82, 150.16, 149.62, 129.87, 126.77, 126.34, 124.69, 122.51, 114.48, 108.42, 71.83, 71.80, 70.26, 70.22, 70.11, 69.51 ppm; ESI-HRMS: *m/z* calcd for $C_{31}H_{32}O_9S_4$: 699.0821 $[M+Na]^+$, found: 699.0822.

Macrocycle exTTFC8

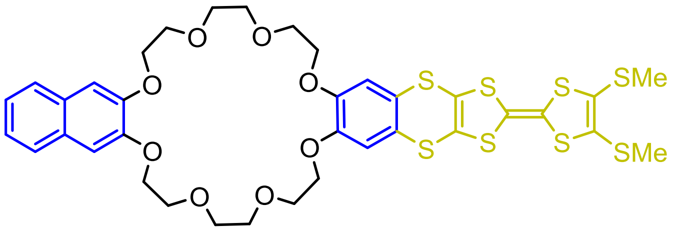

Ketone **3** (105 mg, 155 µmol) and 4,5-bis(methylthio)-1,3-dithiol-2-thione (35.1 mg, 155 µmol) were dissolved in $P(OEt)_3$ (40 mL) and the mixture was heated to 110 °C under argon atmosphere for 3 h. After cooling to room temperature, all volatiles were removed *in vacuo* and the residue was purified by column chromatography (SiO_2, CH_2Cl_2 → CH_2Cl_2/Me_2CO = 20:1). The desired product was obtained as a yellow solid (66.0 mg, 77.2 µmol, 50%). R_f = 0.30 in CH_2Cl_2/MeOH = 100:1; m.p. >189 °C decomposition;^{1}H NMR (700 MHz, CD_2Cl_2): δ = 7.65 (m, 2 H, H_{Ar}), 7.31 (m, 2H, H_{Ar}), 7.12 (s, 2H, H_{Ar}), 6.91 (s, 2H, H_{Ar}), 4.21 (m, 4H, OCH_2), 4.11 (m, 4H, OCH_2), 3.94 (m, 4H, OCH_2), 3.84 (m, 4H, OCH_2), 3.80 (m, 4H, OCH_2), 3.77 (m, 4H, OCH_2), 2.42 (s, 6H, SCH_3) ppm; ^{13}C NMR (176 MHz, CD_2Cl_2): δ = 149.76, 149.63, 129.88, 128.07, 126.97, 126.77, 124.68, 123.96, 116.72, 114.61, 113.33, 108.43, 71.81, 71.76, 70.22, 70.22, 70.13, 69.50, 54.00, 19.64 ppm; ESI-HRMS: *m/z* calcd for $C_{36}H_{38}O_8S_8$: 892.9969 $[M+K]^+$, found: 892.9995.

1.3. Synthesis of rotaxanes R1 and R2

N^1,N^3-bis(4-(prop-2-yn-1-yloxy)benzyl)propane-1,3-diaminium dihexafluorophosphate (A2)

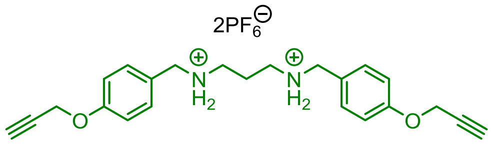

1,3-Diaminopropane (340 µL, 4.0 mmol) and 4-(prop-2-yn-1-yloxy)benzaldehyde (1.28 g, 8.0 mmol) were dissolved in dry EtOH (80 mL) under argon atmosphere and heated to reflux for 6 hours. Afterwards, the mixture was cooled to room temperature and $NaBH_4$ (1.51 g, 40 mmol) was carefully added. The reaction was stirred overnight. Superfluous $NaBH_4$ was quenched by slow addition of a small volume of saturated aqueous $NaHCO_3$ solution. After no gas evolution was observed anymore, all volatiles were removed *in vacuo*. The residue was dissolved in CH_2Cl_2 (50 mL), washed with saturated aqueous $NaHCO_3$ solution (50 mL) and brine (3x50 mL) and dried over $MgSO_4$. After solvent evaporation, the crude product was purified by column chromatograph (SiO_2, CH_2Cl_2 → CH_2Cl_2/MeOH/NEt_3 = 100:10:1). The resulting diamine was transferred to the corresponding hydrochloride by addition of conc. HCl in MeOH (5 mL, 1:1). After drying *in vacuo*, the desired hydrochloride (820 mg, 1.88 mmol) was obtained as a white solid. For the synthesis of the hexafluorophophate salt, part of the hydrochloride (200 mg, 0.46 mmol) and NH_4PF_6 (1.50 g, 9.2 mmol) were dissolved in CH_3CN/water (50 mL, 5:1) and the mixture was stirred for four hours at room temperature. After removing all solvents under reduced pressure, the residue was dissolved in ethyl acetate (100 mL) and washed with water (3x100 mL). Drying over $MgSO_4$ and concentration *in vacuo* yielded the desired product (180 mg, 0.28 mmol, 28% overall yield) as white powder. m.p. 198 °C (decomposition); ^1H NMR (400 MHz, CD_3CN, 298 K): δ = 7.48–7.34 (m, 4H, H_{Ar}), 7.05 (m, 4H, H_{Ar}), 4.77 (d, ^3J = 2.4 Hz, 4H, CH_2), 4.13 (s, 4H, CH_2), 3.15–3.00 (m, 4H, CH_2), 2.84 (t, ^3J = 2.4, 2H, CCH), 2.02 (t, ^3J = 7.8 Hz, 2H, CH_2) ppm; ^{13}C NMR (101 MHz, CD_3CN, 298 K): δ = 159.5, 132.8, 124.0, 116.3, 79.4, 77.2, 56.6, 52.3, 45.5, 23.3 ppm; ESI-HRMS: *m/z* calcd for $C_{23}H_{28}N_2O_2$: 363.2067 $[M-H-2PF_6]^+$, found: 363.2084.

[2]Rotaxane R1

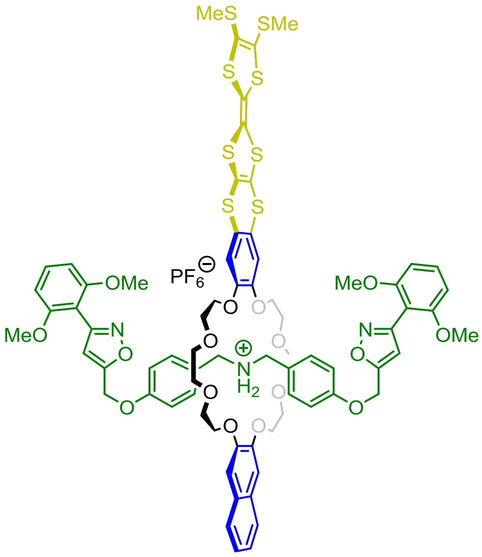

Bis(4-(prop-2-yn-1-yloxy)benzyl)ammonium hexafluorophosphate (4.4 mg, 9.8 μmol) and macrocycle **exTTFC8** (10 mg, 11.7 μmol) were suspended in CH_2Cl_2 (0.5 mL). The mixture was sonicated until the solids were fully dissolved. Afterwards, 2,6-dimethoxybenzonitrile oxide (4.2 mg, 23.4 μmol) was added and the reaction was stirred overnight at 30 °C. The mixture was directly subjected to column chromatography (SiO_2, CH_2Cl_2/MeOH = 250:1). The desired rotaxane **R1** was obtained as an orange solid (10 mg, 6.0 μmol, 61%). R_f = 0.20 in CH_2Cl_2/MeOH = 100:1; ^{1}H NMR (700 MHz, CD_2Cl_2, 298 K): δ = 7.66 (m, 2H, H_{Ar}), 7.44 (s, 2H, NH2), 7.39 (t, ^3J = 8.4 Hz, 2H, H_{Ar}), 7.35 (m, 2H, H_{Ar}), 7.27–7.25 (m, 4H, H_{Ar}), 6.99 (s, 2H, H_{Ar}), 6.83 (s, 2H, H_{Ar}), 6.76– 6.73 (m, 4H, H_{Ar}), 6.67 (d, ^3J = 8.4 Hz, 4H, H_{Ar}), 6.40 (s, 2H, H_{isox}), 4.86–4.81 (m, 4H, OCH_2), 4.62–4.58 (m, 4H, CH_2), 4.18–4.15 (m, 4H, OCH_2), 4.11–4.09 (m, 4H, OCH_2), 3.88–3.86 (m, 4H, OCH_2), 3.82–3.80 (m, 4H, OCH_2), 3.77 (s, 12H, OMe), 3.67–3.64 (m, 4H, OCH_2), 3.60–3.58 (m, 4H, OCH_2), 2.41 (s, 6H, SMe) ppm; ^{13}C NMR (176 MHz, CD_2Cl_2): δ = 166.3, 159.2, 159.1, 157.7, 148.4, 147.8, 131.9, 131.2, 129.7, 128.1, 127.5, 126.9, 125.4, 125.2, 123.8, 117.4, 115.3, 113.2, 112.8, 108.4, 107.4, 107.3, 104.7, 71.6, 71.3, 70.8, 70.7, 69.0, 68.8, 61.3, 56.5, 52.5, 19.6 ppm; ESI-HRMS: *m/z* calcd for $[C_{74}H_{76}N_3O_{16}S_8]^+$: 1518.2991 $[M-PF_6]^+$, found: 1518.3005.

[3]Rotaxane R2

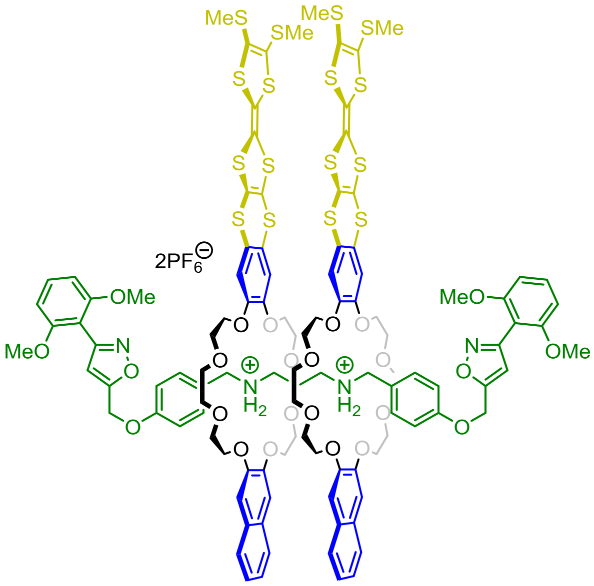

N^1,N^3-Bis(4-(prop-2-yn-1-yloxy)benzyl)propane-1,3-diaminium dihexafluorophosphate (3.3 mg, 5.0 µmol) and macrocycle **exTTFC8** (10 mg, 12.0 µmol) were suspended in 1,2-dichloroethane (1.8 mL). The mixture was sonicated until all solids were completely dissolved. Afterwards, stopper **S1** (2.7 mg, 15.0 µmol) was added and the reaction was stirred for 2 days at room temperature. The mixture was directly subjected to column chromatography (SiO_2, CH_2Cl_2/MeOH = 50:1). The desired product was obtained as an orange solid (5.0 mg, 1.8 µmol, 36%). R_f = 0.5 in SiO_2, CH_2Cl_2/MeOH = 25:1; m.p. >209°C decomposition; ^{1}H NMR (700 MHz, CD_2Cl_2/CD_3CN = 9:1, 298 K): δ = 7.36 (m, 6H, H_{Ar}), 7.11 (m, 8H, NH_2 and H_{Ar}), 7.05 (m, 4H, H_{Ar}), 6.87 (s, 4H, H_{Ar}), 6.72 (s, 4H, H_{Ar}), 6.65 (m, 4H, H_{Ar}), 6.58 (m, 4H, H_{Ar}), 6.32 (s, 2H, $H_{isox.}$), 4.66 (s, 4H, CH_2), 4.37 (m, 4H, $C\underline{H}_2NH_2$), 4.02 (m, 12H, OCH_2), 3.80 (m, 24H, OCH_2), 3.73 (s, 12H, OCH_3), 3.68 (m, 12H, OCH_2), 3.52 (m, 4H, $NH_2C\underline{H}_2CH_2$), 2.38 (s, 12H, SCH_3), 2.02 (m, 2H, $CH_2C\underline{H}_2CH_2$) ppm; ^{13}C NMR (176 MHz, CD_2Cl_2/CD_3CN = 9:1, 298 K): δ = 166.1, 159.1, 158.9, 157.5, 148.0, 147.4, 131.8, 131.2, 129.3, 127.7, 127.5, 126.5, 125.2, 124.1, 123.5, 116.9, 115.2, 113.3, 112.1, 108.8, 107.1, 107.1, 104.5, 71.2, 70.9, 70.6, 70.5, 68.7, 68.5, 61.0, 56.3, 54.0, 45.5, 30.0, 23.0, 19.3 ppm; ESI-HRMS: *m/z* calcd for $C_{113}H_{122}N_4O_{24}S_{16}P_2F_{12}$: 1215.1985 $[M-2PF_6]^{2+}$, found: 1215.1987.

2. Rotaxane characterisation

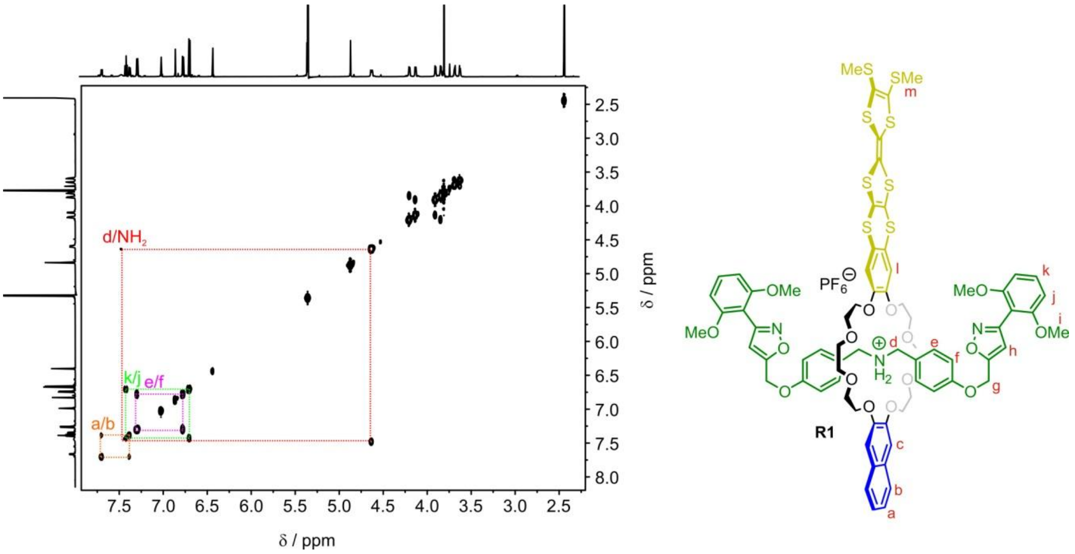

Fig. S1 ^{1}H,^{1}H COSY (700 MHz, CD_2Cl_2, 298 K) of [2]rotaxane **R1** with selected cross peaks confirming the depicted structure.

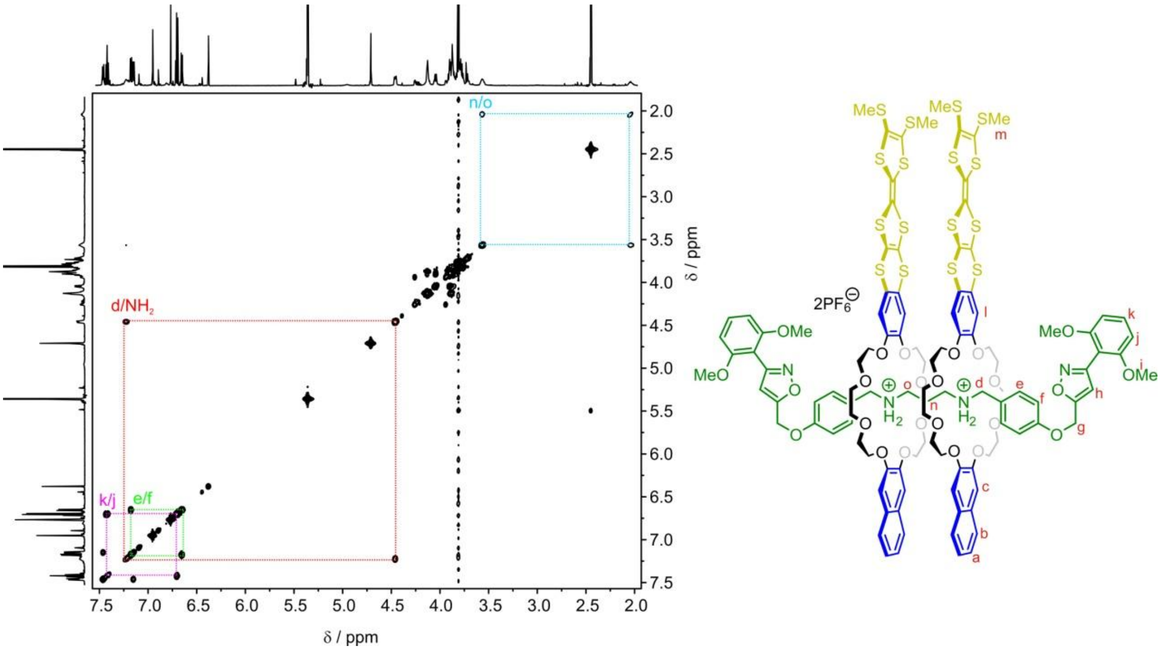

Fig. S2 ^{1}H,^{1}H COSY, (700 MHz, CD_2Cl_2, 298 K) of [3]rotaxane **R2** with selected cross peaks confirming the depicted structure.

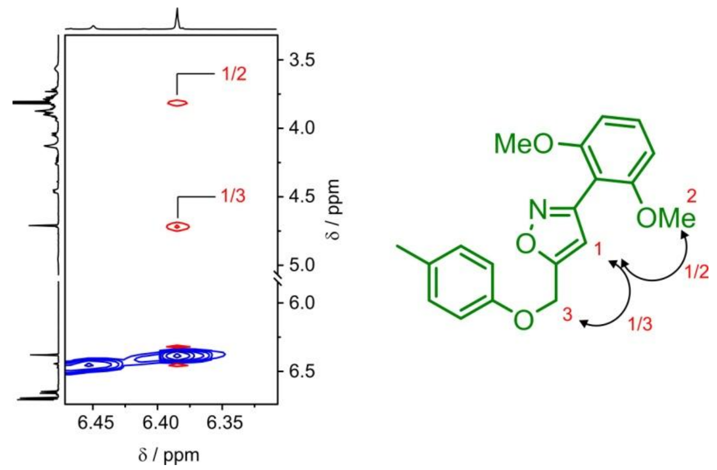

Fig. S3 Partial $^{1}H,^{1}H$ NOESY, (700 MHz, CD_2Cl_2, 298 K) of [3]rotaxane **R2** showing the cross peaks of the isoxazole signal arising by its spatial coupling with neighbouring protons.

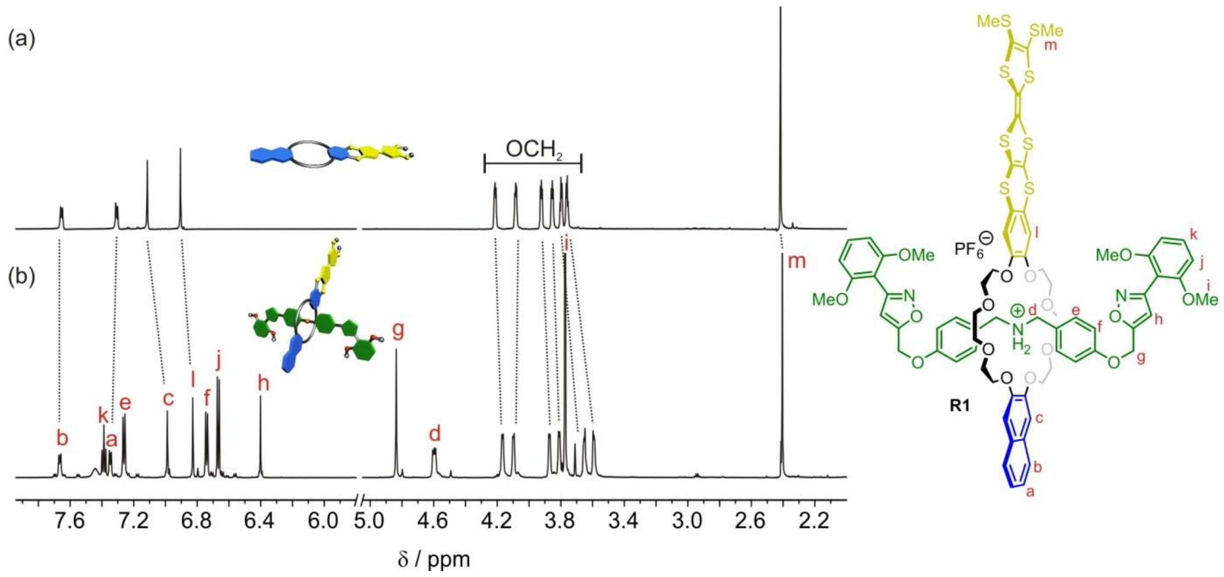

Fig. S4 Stacked ^{1}H NMR spectra (700 MHz, CD_2Cl_2, 298 K) of (a) macrocycle **exTTFC8** and (b) [2]rotaxane **R1** with characteristic signal shifts which can be addressed to a successful rotaxane formation.[S6]

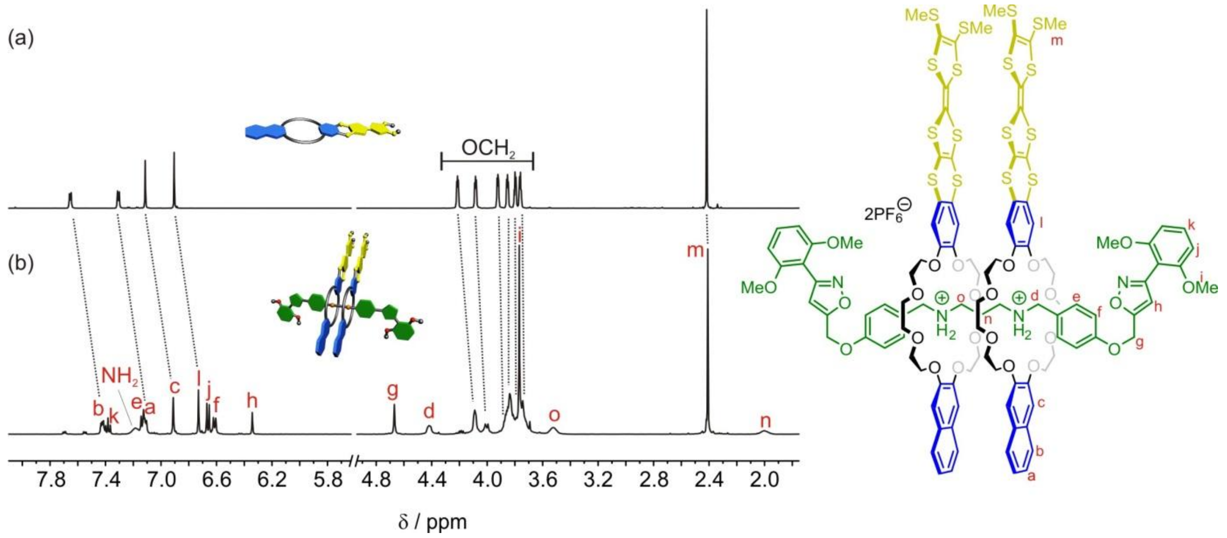

Fig. S5 Stacked ^{1}H NMR spectra (700 MHz, CD_2Cl_2, 298 K) of (a) macrocycle **exTTFC8**, (b) [2]rotaxane **R2** with characteristic signal shifts which can be addressed to a successful rotaxane formation.[S6]

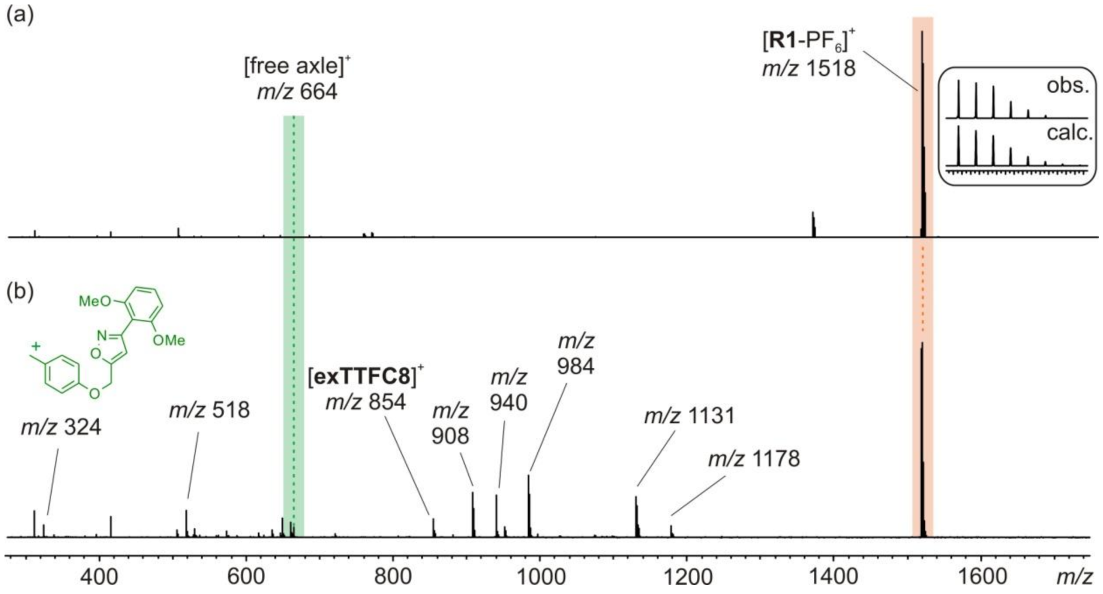

Fig. S6 ESI-FTICR spectra (MeOH, 50 µM, positive mode) of [2]rotaxane **R1**: (a) mass spectrum with base peak *m/z* 1518 (orange area) corresponding to [**R1**-PF_6]$^+$ and (b) mass spectrum after MS/MS IRMPD experiment with selected fragments. The signals *m/z* 854 and *m/z* 324 correspond to the oxidised macrocycle [**exTTFC8**]$^+$ and an axle fragment which results from CN bond breaking in the axle molecule, respectively. The green area indicates the channel for the *m/z* value for the axle without wheel, which is not observed in significant amounts. The fragments between *m/z* 908–1178 are also present in the fragmentation of **R2** and result from different fragmentation channels where an axle piece attacks the wheel. The signal *m/z* 1178, for example, can be addressed to a wheel (*m/z* 854) and the axle fragment (*m/z* 324). This fragmentation pathway speaks in favor of a mechanically interlocked structure as shown previously.[S6]

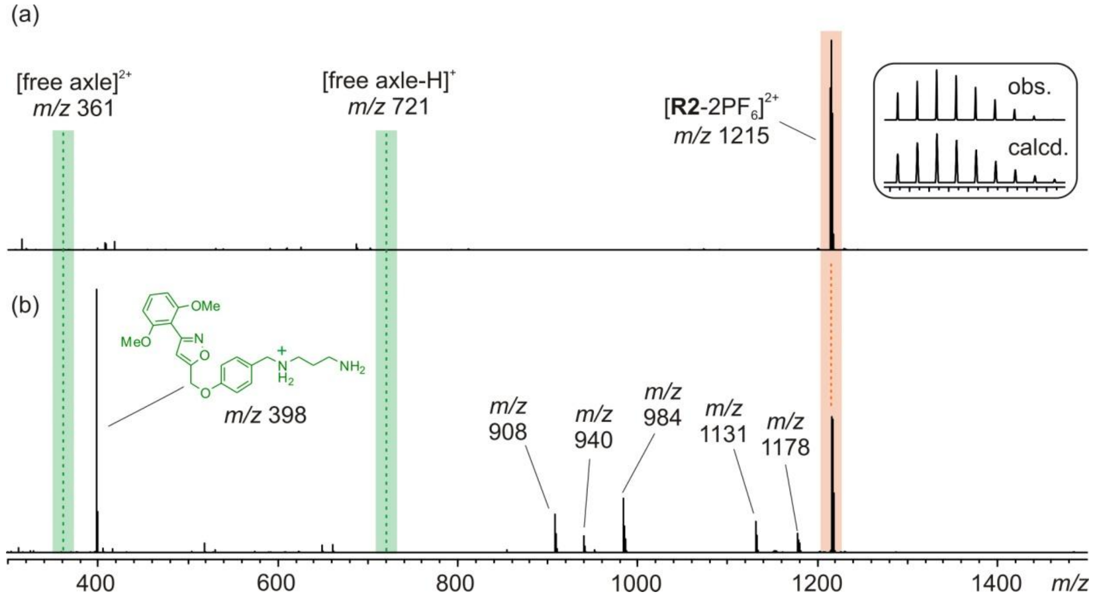

Fig. S7 ESI-FTICR spectra (MeOH, 50 µM, positive mode) of [2]rotaxane **R2**: (a) mass spectrum with base peak *m/z* 1215 (orange area) corresponding to [**R2**-2PF$_6$]$^{2+}$ and (b) mass spectrum after MS/MS IRMPD experiment with selected fragments. The signal *m/z* 398 corresponds to an axle fragment derived by CN bond breaking in the axle molecule. The green area indicates the channel for the *m/z* values for the axle without wheels, which is not observed. The fragments between *m/z* 908–1178 are also present in the fragmentation of **R1** and result from different fragmentation channels where an axle piece attacks the wheel. The signal *m/z* 1178, for example, can be addressed to a wheel (*m/z* 854) and the opposite axle fragment (*m/z* 324). This fragmentation pathway speaks in favor of a mechanically interlocked structure as shown previously.[S6]

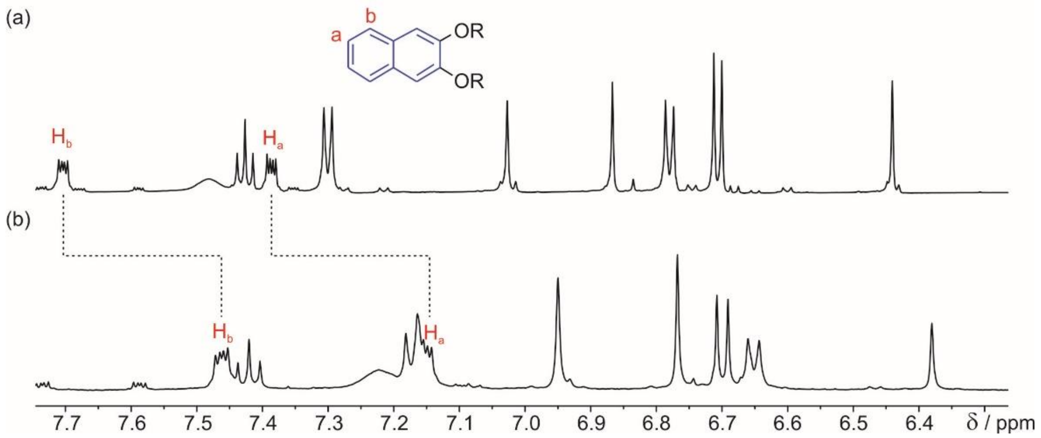

Fig. S8 Comparison of ^{1}H NMR spectra (700 MHz, CD_2Cl_2, 298 K) of (a) [2]rotaxane **R1** and (b) [3]rotaxane **R2** with characteristic signal shifts. For [3]rotaxane **R2**, both naphthalene signals $H_{a/b}$ are significantly shifted by $\Delta\delta$ = -0.24 ppm to higher field. As both rotaxanes are structurally similar, we attribute the quite pronounced upfield shifts of the naphthalene signals H_a and H_b to intramolecular π-stacking interactions between the two wheels in **R2**.

3. UV/Vis-NIR spectroscopy

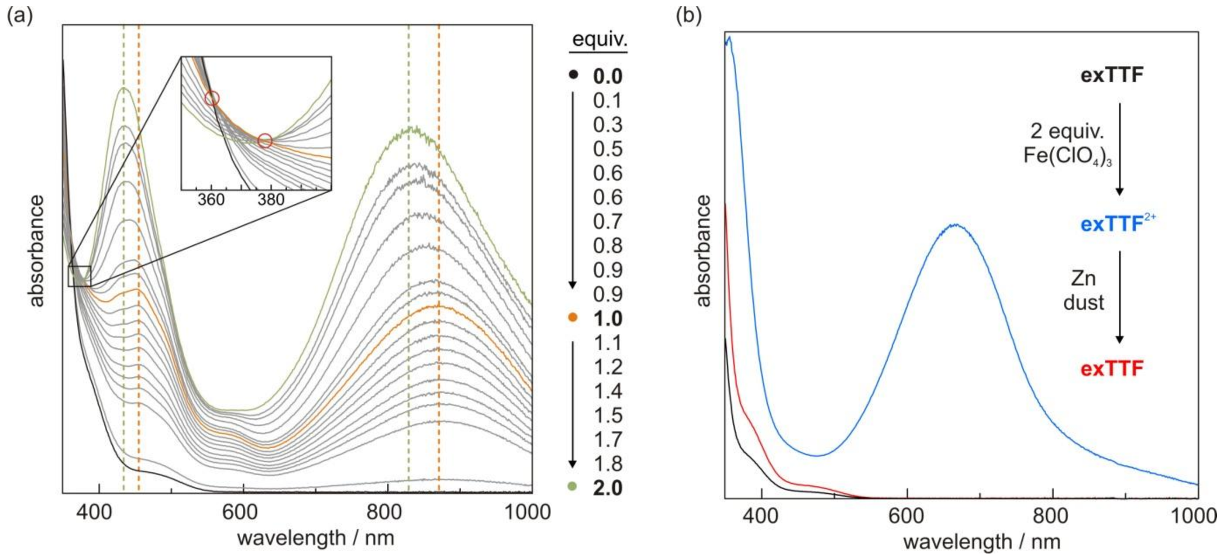

Fig. S9 (a) Photometric UV/Vis titration of **R2** (0.15 mM, CH_3CN, 298 K) by stepwise addition of two equivalents $Fe(ClO_4)_3$. The colored lines corresponds to the UV/Vis spectra of the **R2** (black), **R2**$^{\bullet+}$ (orange) and **R2**$^{2(\bullet+)}$ (green) oxidation state. The dotted lines mark the wavelength of maximum absorbance of the characteristic TTF$^{\bullet+}$ bands. The blue shift going from **R2**$^{\bullet+}$ to **R2**$^{2(\bullet+)}$ is known as “Davydov blue shift” which is characteristic for cofacial TTF radical-cation dimers.[S7] This is additionally supported by two isosbestic points (inset) which are in accordance to two separate transitions **R2**/**R2**$^{\bullet+}$ and **R2**$^{\bullet+}$/**R2**$^{2(\bullet+)}$. (b) UV/Vis spectra of redox-active building block **exTTF** (5×10^{-5} M, CH_3CN/CH_2Cl_2 (2:1), 298 K): before oxidation (black), after addition of two equivalents $Fe(ClO_4)_3$ (blue), and (iii) after back reduction by addition of excess Zn dust (red).

4. Isothermal titration calorimetry

ITC titrations were carried out in mixtures of dry 1,2-dichloroethane and acetonitrile (10:1) at 298 K on a TAM III microcalorimeter (Waters GmbH, TA Instruments, Eschborn, Germany). In a typical experiment, a solution of macrocycle (800 µL, 1 mM) was placed in the sample cell and a solution of the ammonium salt (250 µL, 8 mM) was put into a syringe. Titrations consisted of 32 consecutive injections of 8 µL, each with a 15 min interval between injections. Heats of dilution were determined by titration of ammonium salt solutions into the sample cell containing blank solvent and were subtracted from each data set. The heat flow generated in the sample cell is measured as a differential signal between sample and reference cell. Hence, an exothermic event results in a positive and an endothermic in a negative heat flow. The data were analysed using the instrument’s internal software package and fitted with a 1:1 or 1:2 binding model. Each titration was conducted three times and the measured values for *K*, Δ*G* and Δ*H* were averaged.

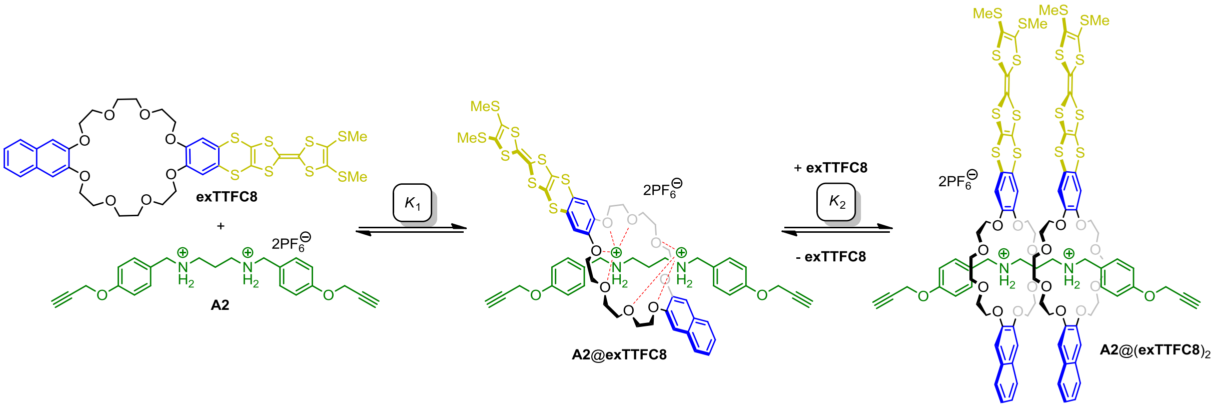

Fig. S10 Schematic representation of the two binding steps (with association constants K_1 and K_2) in the divalent pseudo[3]rotaxane **A2@(exTTFC8)**$_2$.

The trends in thermodynamic parameters in the pseudo[3]rotaxanes **A2@(exTTFC8)**$_2$ and **A2@(DBC8)**$_2$ can be explained by different effects. Considering statistics, a ratio between the binding constants of the monovalent (e.g. **A1@exTTFC8**) and divalent complex (e.g. **A2@(exTTFC8)**$_2$) of $K = K_1/2 = 2K_2$ is expected if no communication between the two binding sites occurs (non-cooperative binding). However, the ammonium binding station in the divalent axle **A2** is assumed to bind weaker to the wheel than the monovalent one due to the absence of a second polarisable benzylic methylene group. The observation that K_1 is roughly two times *K* is explained in Figure S10. We assume that the first wheel partially binds to both binding stations. Thus, the second ammonium station site is blocked for the second binding event and a lower K_2 value can thus easily be rationalised by the competition between the first and the second macrocycle for the second station. The high enthalpic gain of the second binding event, in case of **exTTFC8** macrocycle, can be attributed to rather strong attractive wheel-wheel interactions. On the other hand, this comes together with the high entropic penalty, as the conformation of the two crown ether macrocycles for additional wheel-wheel interactions is very rigid.

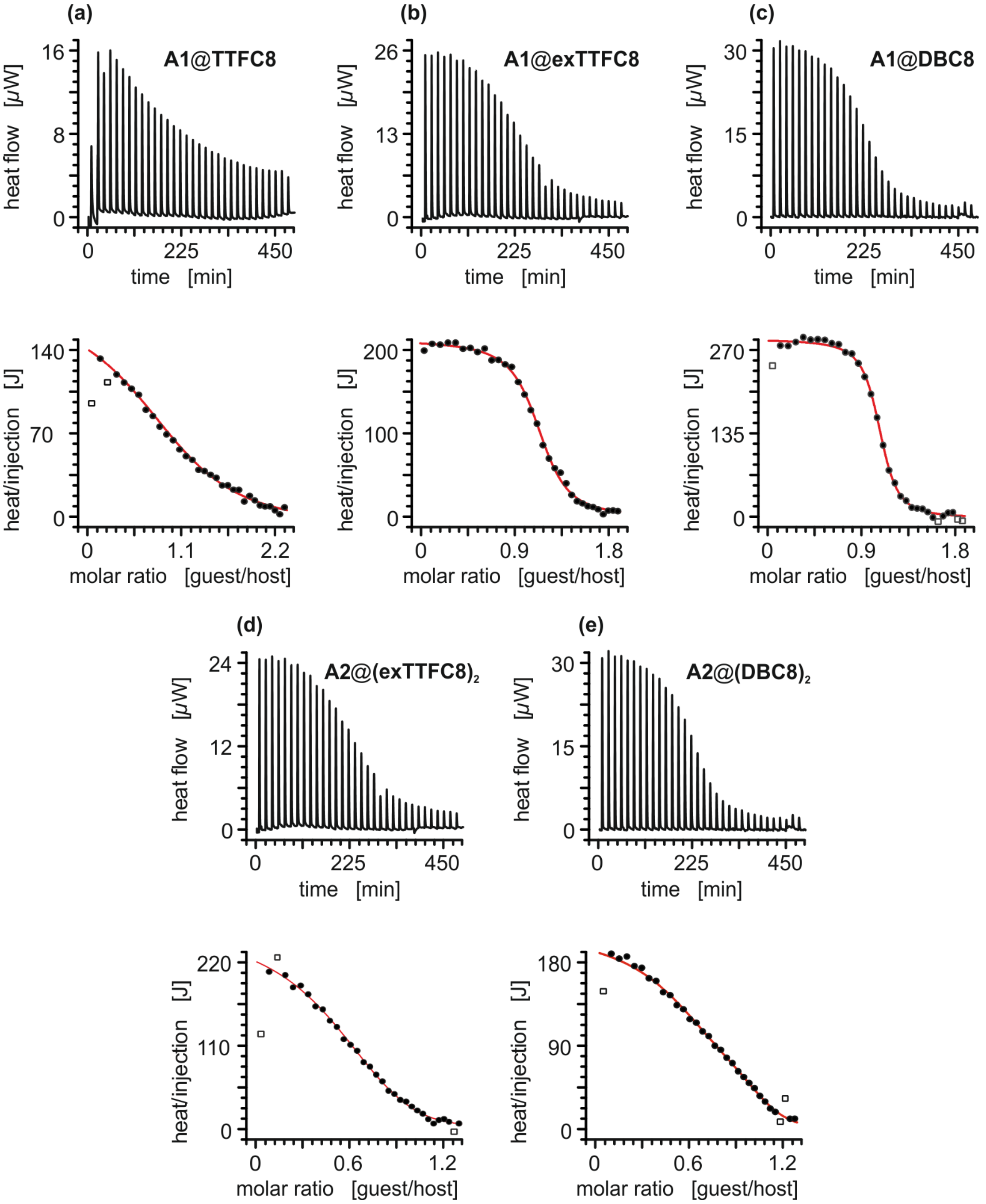

Fig. S11 Titration plots (heat flow versus time and heat/volume versus guest/host ratio) obtained from ITC experiments at 298 K in 1,2-dichloroethane/acetonitrile 10:1 (v/v). Concentrations: (a) host: 0.96 mM, guest: 7.7 mM; (b) host: 1.03 mM, guest: 6.0 mM; (c) host: 1.22 mM, guest: 7.6 mM; (d) host: 0.87 mM, guest: 3.2 mM; (e) host: 0.87 mM, guest: 3.3 mM; Points marked with a non-filled square were not included in the fitting process.

Table S1. Thermodynamic binding data of pseudo[2]- and [3]rotaxane formation between axles (**A1** and **A2**) and macrocycles (**exTTFC8**, **TTFC8**, and **DBC8**) obtained from ITC experiments in 1,2-dichloroethane/acetonitrile (10:1) at 298 K.

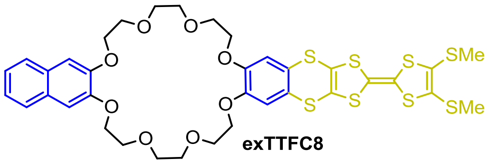
exTTFC8

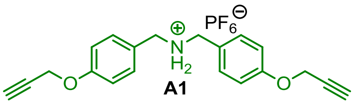
A1

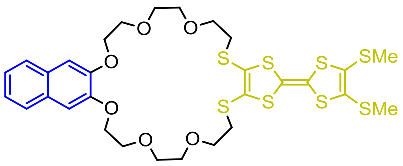
TTFC8

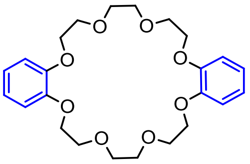
DBC8

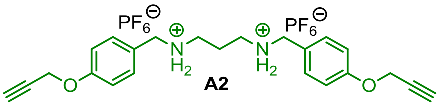
A2

		K_n / 10^3 M^{-1}	ΔG / kJ mol^{-1}	ΔH / kJ mol^{-1}	$T\Delta S$ / kJ mol^{-1}
A1⊂exTTFC8	K_1	50 ± 5	-26.8 ± 0.2	-36.8 ± 1.2	-10.0 ± 1.4
A1⊂TTFC8	K_1	3.8 ± 0.4	-20.4 ± 0.3	-23.3 ± 0.4	-2.8 ± 0.7
A1⊂DBC8	K_1	90 ± 9	-28.3 ± 0.2	-35.7 ± 1.8	-8.0 ± 2.0
A2⊂(exTTFC8)$_2$	K_1	99 ± 30	-28.5 ± 0.7	-32.6 ± 1.0	-4.1 ± 1.7
	K_2	2.4 ± 0.6	-19.3 ± 0.5	-45.4 ± 4.3	-26.1 ± 4.8
A2⊂(DBC8)$_2$	K_1	180 ± 40	-30.0 ± 0.5	-35.6 ± 1.3	-5.6 ± 1.8
	K_2	2.7 ± 0.6	-19.5 ± 0.5	-31.1 ± 4.9	-11.7 ± 5.4

5. Cyclic voltammetry and digital simulations

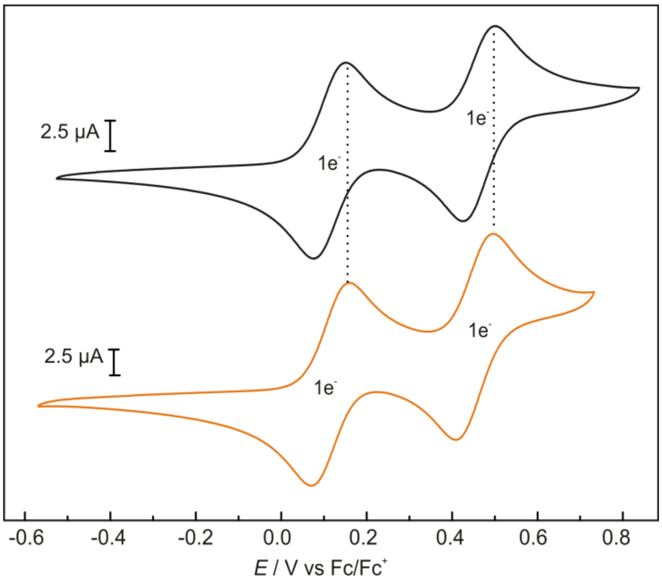

Fig. S12 Cyclic voltammograms (CH_2Cl_2, 298 K, 1 mM, 100 mV s^{-1}) of macrocycle **exTTFC8** (top) and [2]rotaxane **R1** (bottom). The potential were referenced against the ferrocene/ferrocenium (Fc/Fc^+) couple as described earlier.[S8] No significant difference in half-wave potentials is observed for the CH_2Cl_2 measurement which indicates that the charge repulsion between oxidised macrocycle and ammonium axle in **R1** does not play a significant role.

Digital simulations. The cyclic voltammogram of **R2** was simulated with the DigiElch Professional software (ElchSoft GbR) using the Butler-Volmer equation. The surface area of the working electrode was set to 0.14 cm^2 and the starting concentration of **R2** was set to 1 mM. The charge-transfer coefficients α were at the initial value of 0.5 and the heterogeneous rate constants k_s were estimated by the peak separation and set between 0.001 and 0.01 cm^2 s^{-1}. The diffusion coefficient was roughly estimated by fitting the experimental electrochemical data and set to $1x10^{-10}$ m^2 s^{-1}.

The electrochemical reaction mechanism of **R2** can be described by an eight-member square scheme as depicted in Scheme 1. In each oxidation state, the electrochemical equilibrium is coupled with a reversible interaction (C1–C4) between the two wheels in **R2**. The wheel-wheel interactions (ΔG) result in an intramolecular binding constant K_{Cm} (m = 1–4). On the left side of the square scheme, the species marked with an asterisk (($\mathbf{R2}^{n+}$)*; n = 0, 1, 2, or 4) are representing an unbound situation in which wheel-wheel interaction are absent. The left side ($\mathbf{R2}^{n+}$) displays the bound situation in which wheel-wheel interactions—such as attractive dispersion interactions or charge repulsion—are present. If all K_{Cm} values would be negligible ($\Delta G \approx 0$), the intramolecular equilibrium is mainly on the side of the noninteracting species $(\mathbf{R2}^{n+})^*$. This would be true, for example, if both wheels are widely separated by a long spacer and cannot form any type of interaction. Consequently, the potentials should be similar to those of monovalent [2]rotaxane **R1** (E1*–E3*) where all intramolecular wheel-wheel interaction can be fully excluded. If the $K_{\mathrm{C}m}$ values are significant, however, the $\mathbf{R2}^{n+}$ states are more populated which results in an altered voltammetric response (E1–E3).

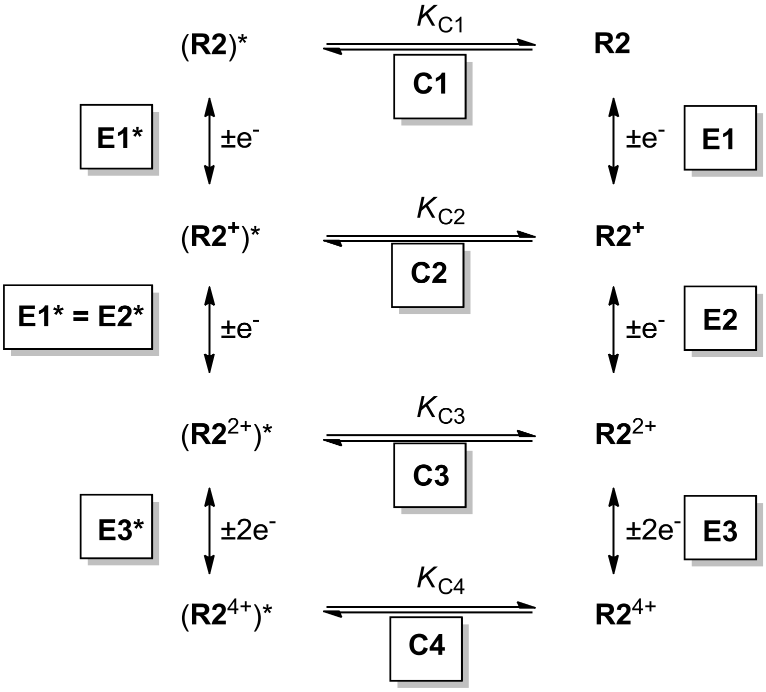

Scheme S2 Square scheme of the electrochemical reaction mechanism of **R2**

The experimental data were fitted according the following equilibria:

$(\mathbf{R2})^*$		$\rightleftharpoons$	$\mathbf{R2}$		(C1)
$(\mathbf{R2}^{\bullet+})^*$		$\rightleftharpoons$	$\mathbf{R2}^{\bullet+}$	MV Dimer	(C2)
$(\mathbf{R2}^{2(\bullet+)})^*$		$\rightleftharpoons$	$\mathbf{R2}^{2(\bullet+)}$	RC Dimer	(C3)
$(\mathbf{R2}^{4+})^*$		$\rightleftharpoons$	$\mathbf{R2}^{4+}$		(C4)
$(\mathbf{R2}^{\bullet+})^*$	$+e^-$	$\rightleftharpoons$	$(\mathbf{R2})^*$	(0.16 V)	(E1*)
$(\mathbf{R2}^{2+})^*$	$+e^-$	$\rightleftharpoons$	$(\mathbf{R2}^{\bullet+})^*$	(0.16 V)	(E2*)
$(\mathbf{R2}^{4+})^*$	$+2e^-$	$\rightleftharpoons$	$(\mathbf{R2}^{2(\bullet+)})^*$	(0.40 V)	(E3*)
$\mathbf{R2}^{\bullet+}$	$+e^-$	$\rightleftharpoons$	$\mathbf{R2}$	(0.08 V)	(E1)
$\mathbf{R2}^{2(\bullet+)}$	$+e^-$	$\rightleftharpoons$	$\mathbf{R2}^{\bullet+}$	(0.19 V)	(E1)
$\mathbf{R2}^{4+}$	$+2e^-$	$\rightleftharpoons$	$\mathbf{R2}^{2(\bullet+)}$	(0.48 V)	(E1)

The fitting and simulation process is based on several assumptions (see above) and involves a large number of fitting parameters. It is therefore important to emphasise that the computational model only gives a qualitative picture of the K_{Cm} values (wheel-wheel interactions) in the present situation.[S9] The applied model results in the following qualitative order of binding constants:

$$K_{C2}\ (\mathbf{R2}^{\bullet+}) > K_{C3}\ (\mathbf{R2}^{2(\bullet+)}) > K_{C1}\ (\mathbf{R2}) >> K_{C4}\ (\mathbf{R2}^{4+})$$

Furthermore, the model provides a rough estimate of the constant's relations:

$$K_{C1} \approx K_{C2}/18 \approx K_{C3}/4 \approx K_{C4}/0.01$$

In Figure S12, the effect of varying the absolute value of a binding constant on the simulated cyclic voltammogram is demonstrated using K_{C2} as example. A value of K_{C2} = 10 leads to a voltammetric response obviously different from the experimental one. By going to higher K_{C2} values, the model provides a good simulation at $K_{C2} \approx 1000$. However, a further increase does not significantly influence the simulated cyclic voltammogram. This demonstrates that the present computational model, based on the proposed mechanism, can reproduce the experimental data, but is insufficient to determine reliable quantitative thermodynamic and kinetic values.

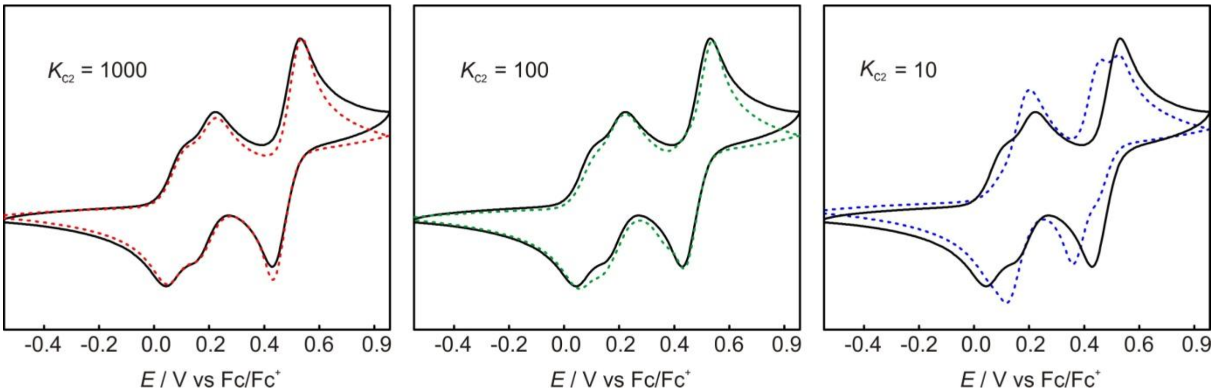

Fig. S13 Experimental cyclic voltammogram of **R2** (black trace, 100 mV s^{-1}, CH_3CN, 1 mM, 298 K) with n-Bu_4NPF_6 (0.1 M) as the electrolyte and simulated cyclic voltammograms with different values of the intramolecular binding constant K_{C2}.

6. IM-MS

Instrumentation and CCS determination. Ion mobility analysis was carried out by means of a home-built drift tube ion mobility-mass spectrometry (IM-MS) instrument (Fig. S14).[S10] Briefly, ions are generated by a nanoelectrospray ionisation (nESI) source (positive ion mode) and transferred into an ion funnel from which the ions are pulsed into the drift tube region (length = 80.55 cm). Guided by a weak electric field the ions traverse the drift tubes, which are filled with a neutral buffer gas (helium, 4.18 mbar, 23.4 °C). The time required for the ions to pass the drift tube region depends on their mobility, which in turn is dictated by the molecules' overall shape and charge. Compact molecules undergo fewer collisions with the buffer gas and traverse the drift tube region faster than more extended structures of same mass-to-charge ratio (*m/z*). The ions become subsequently guided by a second ion funnel into high vacuum where the ions are selected according to their *m/z* by means of a quadrupole mass analyser. The arrival time distributions (ATDs) of the ions are recorded by measuring the time that ions of a specific *m/z* need to traverse the drift region. The time which corresponds to the intensity maximum of the ATD was taken as the drift time (t_D). The t_D values were determined for different drift voltages (V_D) and plotted against $1/V_D$. The data were fitted to a linear function (Fig. S15b). As described previously, the slope of the linear fit was used to calculate the mobility of the ion from which finally the collision cross section (CCS) could be determined by using the Mason-Schamp equation.[S11,12]

Calculations. The calculated CCS values of model conformers of [3]rotaxane **R2** without PF_6^- counter ions (**A**–**H**) were obtained by the projection approximation (PA) method.[S13] For the conformer search, we structurally optimised different wheel coconformations (**C**–**H**) using the semi-empirical PM3 method as implemented in the ORCA 3.0.3 program package (Fig. S16).[S14,15] The conformers **A** and **B**—which were further optimised by the MMFF94 force field as implemented in the Avogadro[S15,16] 1.1.1 software—are representing a *syn* coconformation in which the stopper groups are either tightly wrapped around the stacked wheels (**A**) or off-standing (**B**).

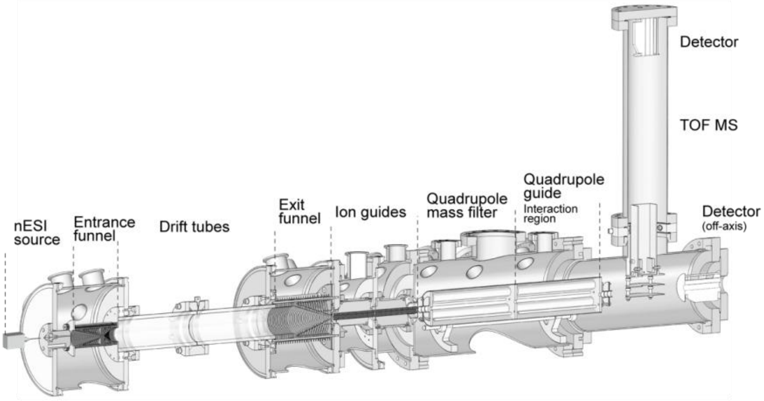

Fig. S14 Instrumental setup of the drift tube ion mobility mass spectrometer.[S10]

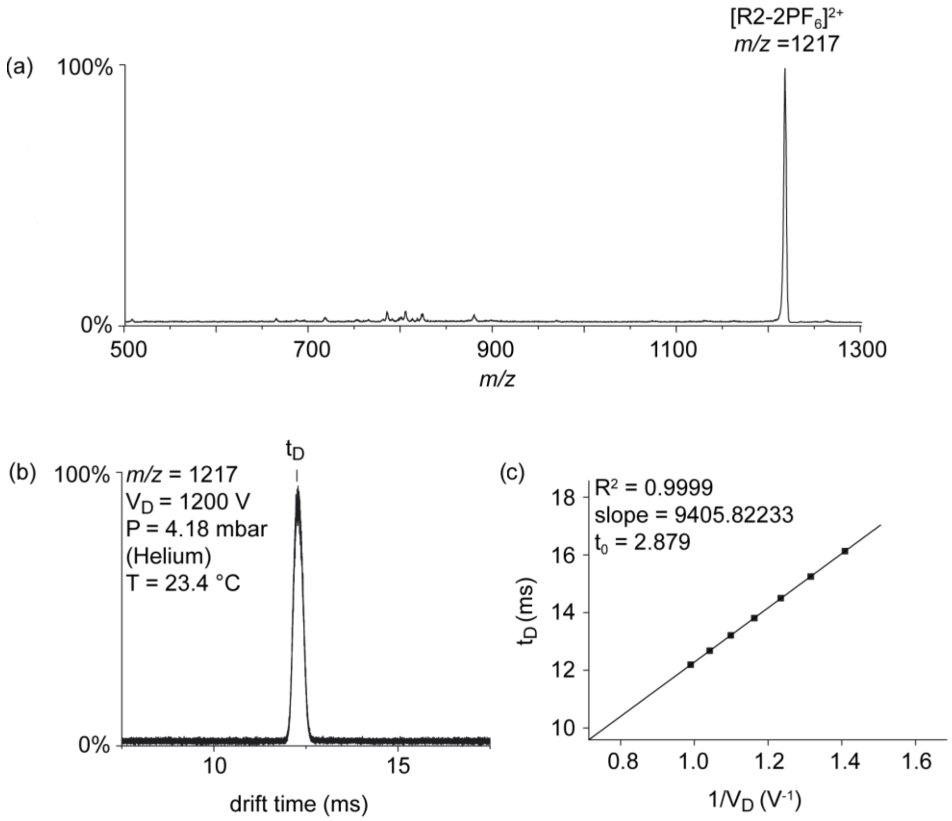

Fig. S15 Overview of IM-MS data: (a) nESI(+)-MS spectrum of **R2** sprayed from CH_2Cl_2, (b) Representative ATD obtained from the [**R2**-$2PF_6$]$^{2+}$ ion (m/z = 1217), (c) Drift time (t_D) values that were determined for the [**R2**-$2PF_6$]$^{2+}$ ion population at different drift voltages (V_D) and plotted against $1/V_D$. The offset (t_0 - interception with the y-axis) is the time required for the ions to travel from the exit of the drift tubes to the detector.

Table S2 Comparison of experimental CCS of [**R2**-$2PF_6$]$^{2+}$ (m/z 1217) to theoretical CCS values of optimised conformer structures (**A–H**) depicted in Figure S15.

ion	**CCS$_{exp}$** / Å^2	**Conformer**	**CCS$_{calcd}$** / Å^2	**Deviation** / %
[**R2**-$2PF_6$]$^{2+}$	410	A	412.2	0.5
		B	464.2	13.2
		C	472.2	15.2
		D	472.4	15.2
		E	472.6	15.3
		F	477.7	16.5
		G	491.0	19.8
		H	498.2	21.5

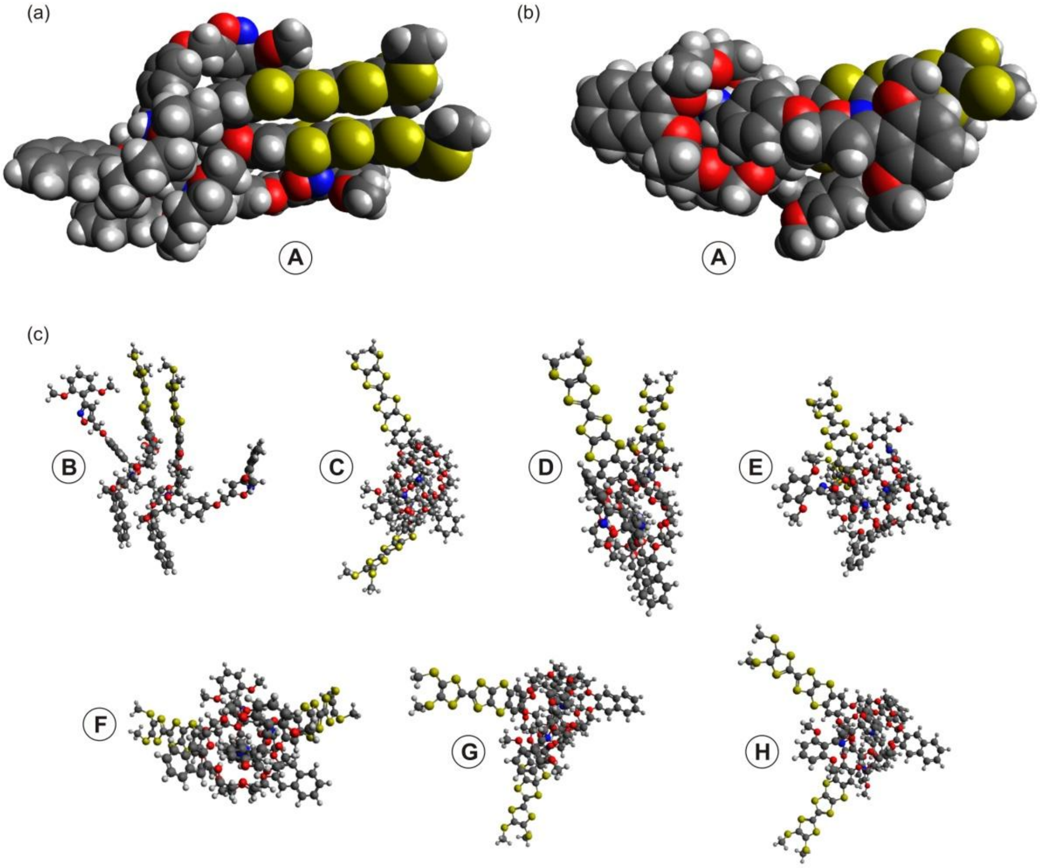

Fig. S16 PM3 (**C**–**H**) or force-field-optimised (**A** and **B**) conformers of [3]rotaxane **R2** without PF_6^- counter ions. (a) Side-view and (b) top-view of conformer **A** with *syn* coconformation of the wheels. The molecules are depicted as Van der Waals sphere models. (c) Ball and stick models of conformers **B**–**H**.

7. VT-NMR

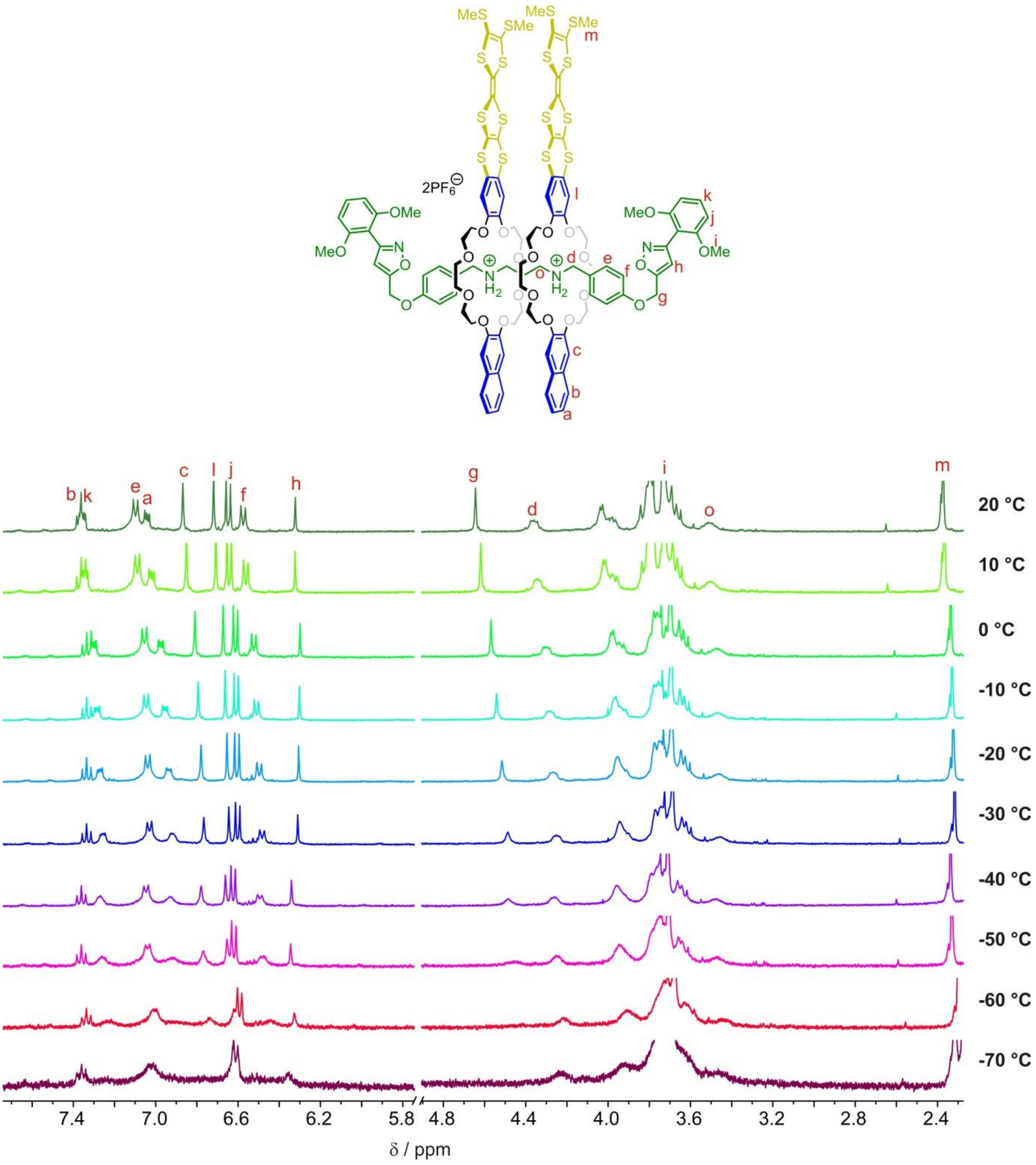

Fig. S17 ^{1}H NMR spectra (400 MHz, CD_2Cl_2/CD_3CN = 9:1, 1.0 mM) of **R2** with gradual cooling from 20 to -70 °C. No signal decoalescence was observed which indicates a fast rotamer interconversion and, thus, a low barrier for the pirouetting motion of the clutched wheels of **R2**.

8. Computational details

Structural ground-state aspects of *syn* and *anti* R2. All calculations were performed using the program package Turbomole (Version 7.0.1).[S18] Structure optimisations were carried out at the TPSS-D3(BJ)/def2-SVP[S19-22] level of DFT employing the RIJ-approximation[S23,24] together with its multipole acceleration extension (MARIJ)[S25] and regarding implicit solvent effects with COSMO[S26] ($\varepsilon = 36.64$ for MeCN). We used a computer-time-reducing, stopper-less pseudorotaxane analogue. During the first two oxidation processes in *syn* **R2**, the interplanar distance between the TTF units decreases from 3.14 Å to 3.09 Å while the distance between the stacked naphthalene moieties remains rather constant around 3.32 Å. However, the last oxidation in *syn* **R2** results in a significant increase of the TTF-TTF distance (from 3.09 Å to 3.17 Å) and a notable decrease of the naphthalene dimer separation (from 3.32 Å to 3.16 Å). This corresponds to an influence being exerted by the naphthalene moieties on the electronic structure of *syn* **R2** upon the last oxidation process and relates to the unfavorable molecular structure of *syn* **R2**$^{4+}$ in comparison to *anti* **R2**$^{4+}$. In contrast to *syn* **R2**, the interplanar distances in *anti* **R2** are only slightly altered upon oxidation (going from 3.31 Å in *anti* **R2** to 3.27 Å in *anti* **R2**$^{4+}$). Furthermore, *anti* **R2** displays a triply π-stacked system at one side, while the other is a somewhat distorted TTF-naphthalene dimer (see Fig. 7).

Electronic structure and energetic aspects. Single point calculations at the relaxed geometries were performed at the PBE0-D3(BJ)/def2-TZVP[S27] level using COSMO ($\varepsilon = 36.64$ for MeCN). The molecular orbitals obtained at this level of theory suggest that in each oxidation state the valence electronic structure of *syn* **R2** is dominated by the TTF dimer (see Fig. 6 for *syn* **R2**$^{\bullet+}$ and *syn* **R2**$^{2(\bullet+)}$). In *anti* **R2** on the other hand, the single TTF units both participate in the valence electronic structure, albeit without the non-covalent interactions between the moieties. Table S3 compares the calculated ionisation potentials to the experimentally determined values by CV. Since the CV measurement is considerably slower than the intramolecular rearrangements that constitute the switching from *syn* **R2** to *anti* **R2**, the energy of the rearrangement process between the two conformers is taken into account for the first (**R2/R2**$^{\bullet+}$) and third (**R2**$^{2(\bullet+)}$**/R2**$^{4+}$) oxidation process. As seen in Table S3, no rearrangement needs to be considered for the second oxidation process (**R2**$^{\bullet+}$/ **R2**$^{2(\bullet+)}$). An overall decent agreement between experiment and theory is observed, especially in the case of the second oxidative process, which does not require any consideration about intramolecular rearrangements. The other processes do display small deviations from experimental values. This might be in parts due to the somewhat superficial treatment of the rearrangement energy and, moreover, due to inherent inaccuracies of the method.

Table S3 Calculated and experimental ionisation potentials (in eV) of **R2**. $\mathbf{IP_0}$ denotes the ionisation potential computed via $\mathbf{IP_0} = E(N) - E(N\text{-}1)$, where E is the ground state energy of the structurally relaxed compound. $\mathbf{IP_{rearr}}$ regards the rearrangement between *syn* **R2** and *anti* **R2** via $\mathbf{IP_{rearr}} = \mathbf{IP_0} + \Delta E_{\text{syn/anti}}$, where $\Delta E_{\text{syn/anti}}$ denotes the ground state energetic difference between the relaxed *syn* and *anti* structure. Experimental values are obtained by referencing the CV data to the Fc/Fc$^+$ couple according to $\mathbf{IP_{exp}} = (-(E_{1/2})/\text{V} - 4.80)$ eV, where $E_{1/2}$ is the half-wave potential of the oxidation peak.

Oxidation	$\mathbf{IP_0}$	$\mathbf{IP_{rearr}}$	$\mathbf{IP_{exp}}$
R2/R2$^{\bullet+}$	4.43	4.76	4.88
R2$^{\bullet+}$/**R2**$^{2(\bullet+)}$	4.98	4.98*	4.99
R2$^{2(\bullet+)}$/**R2**$^{4+}$	6.13	5.62	5.29

[a] No rotation occurs.

Rotational motion. In order to mimic the gear slippage motion of **R2** in its four oxidation states, one of the macrocycles was displaced against the other in steps of 45° (Fig. S18). At every position a restricted optimisation was performed by fixing the coordinates of the central C-C bond in each TTF unit to obtain an intermediate structure on the way between *syn* **R2** and *anti* **R2**. The method employed for the optimisation was the semi-empirical HF-3c approach recently proposed by Grimme,[S28] as conventional methods (e.g., TPSS-D3(BJ)) failed to converge the structures. The potential energy curves depicted in Fig. 7b were received at the PBE0-D3(BJ)/def2-TZVP level using COSMO[S26] (ε = 36.64 for MeCN).

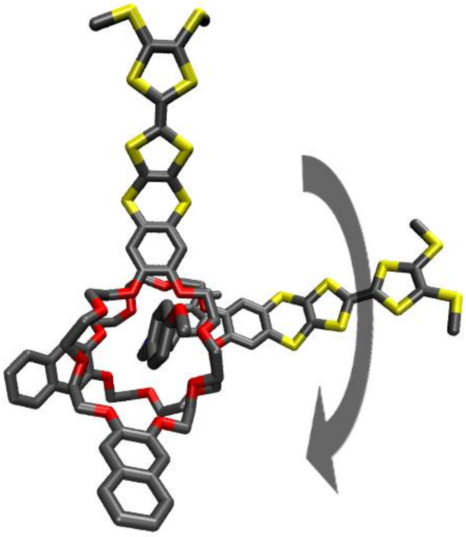

Fig. S18 Example for an intermediate structure between syn and *anti* **R2** (90°). The arrow indicates the rotational motion accomplished by displacing one macrocycle against the other. A computer-time-reducing, stopper-less pseudorotaxane analogue is used.

9. ^{1}H and ^{13}C NMR spectra

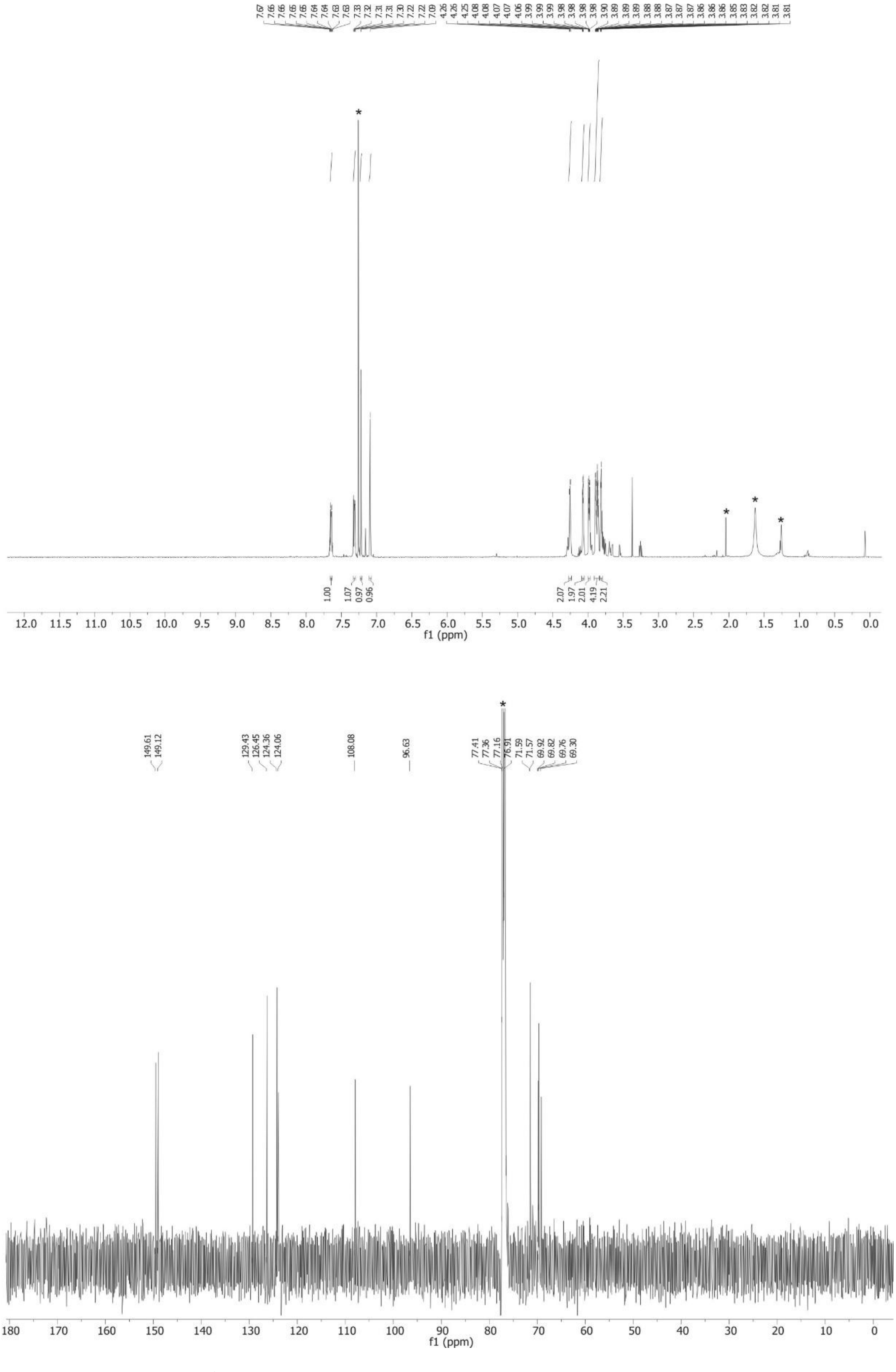

Fig. S19 ^{1}H and ^{13}C NMR spectrum (500/126 MHz, $CDCl_3$, 298 K) of diodide **1**.

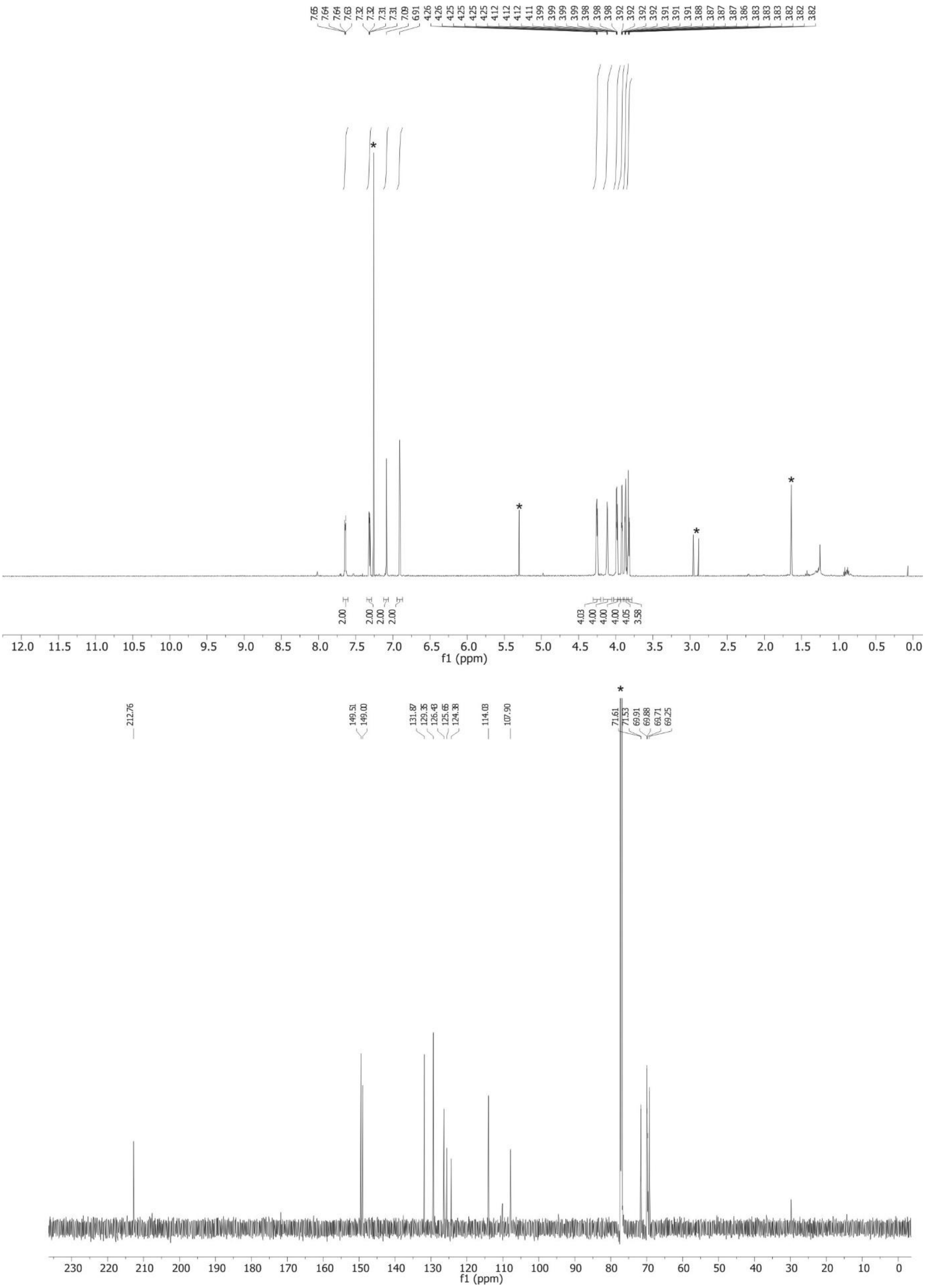

Fig. S20 ^{1}H and ^{13}C NMR spectrum (700/176 MHz, $CDCl_3$ 298 K) of thione **2**.

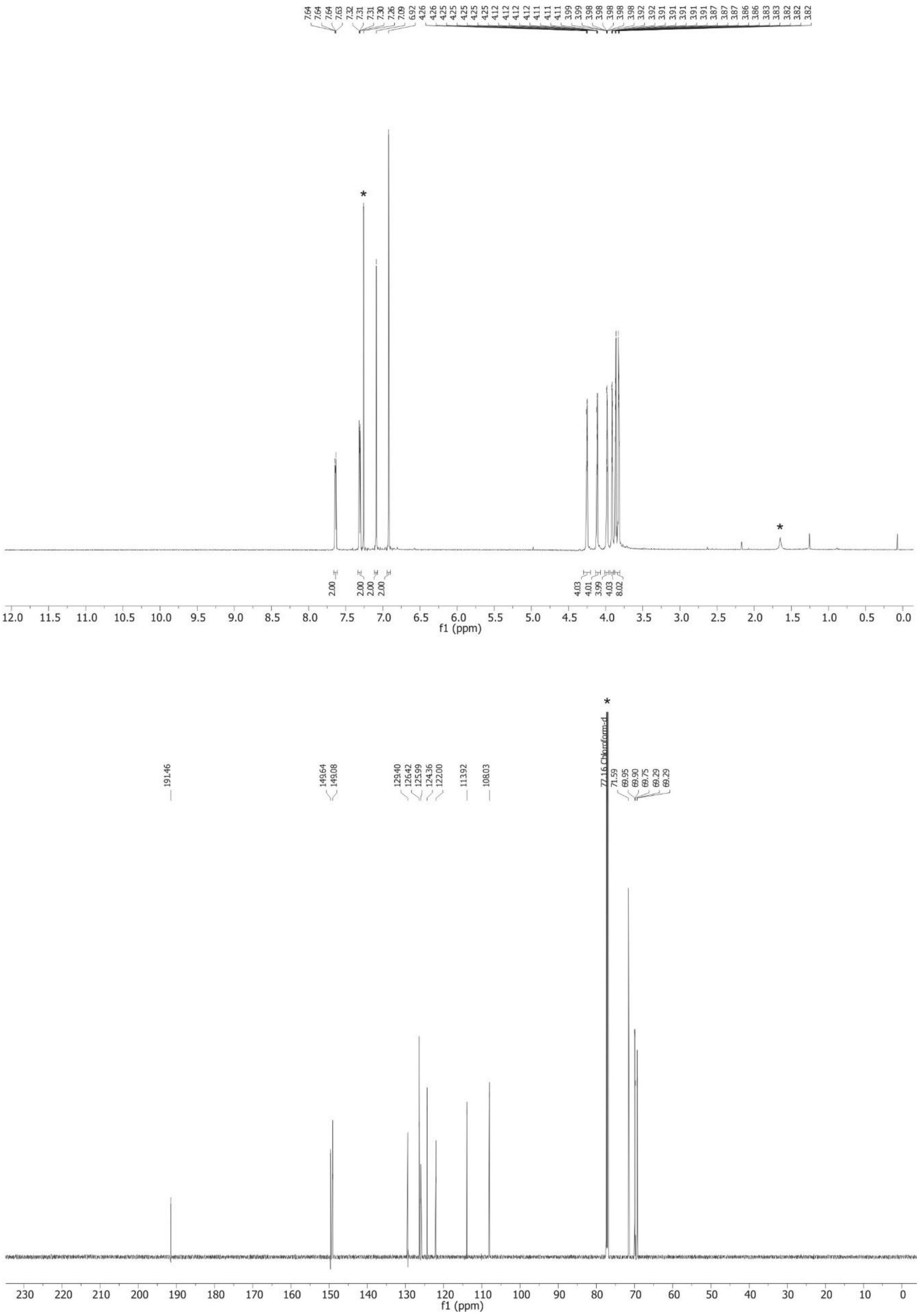

Fig. S21 ^{1}H and ^{13}C NMR spectrum (700/176 MHz, $CDCl_3$ 298 K) of ketone **3**.

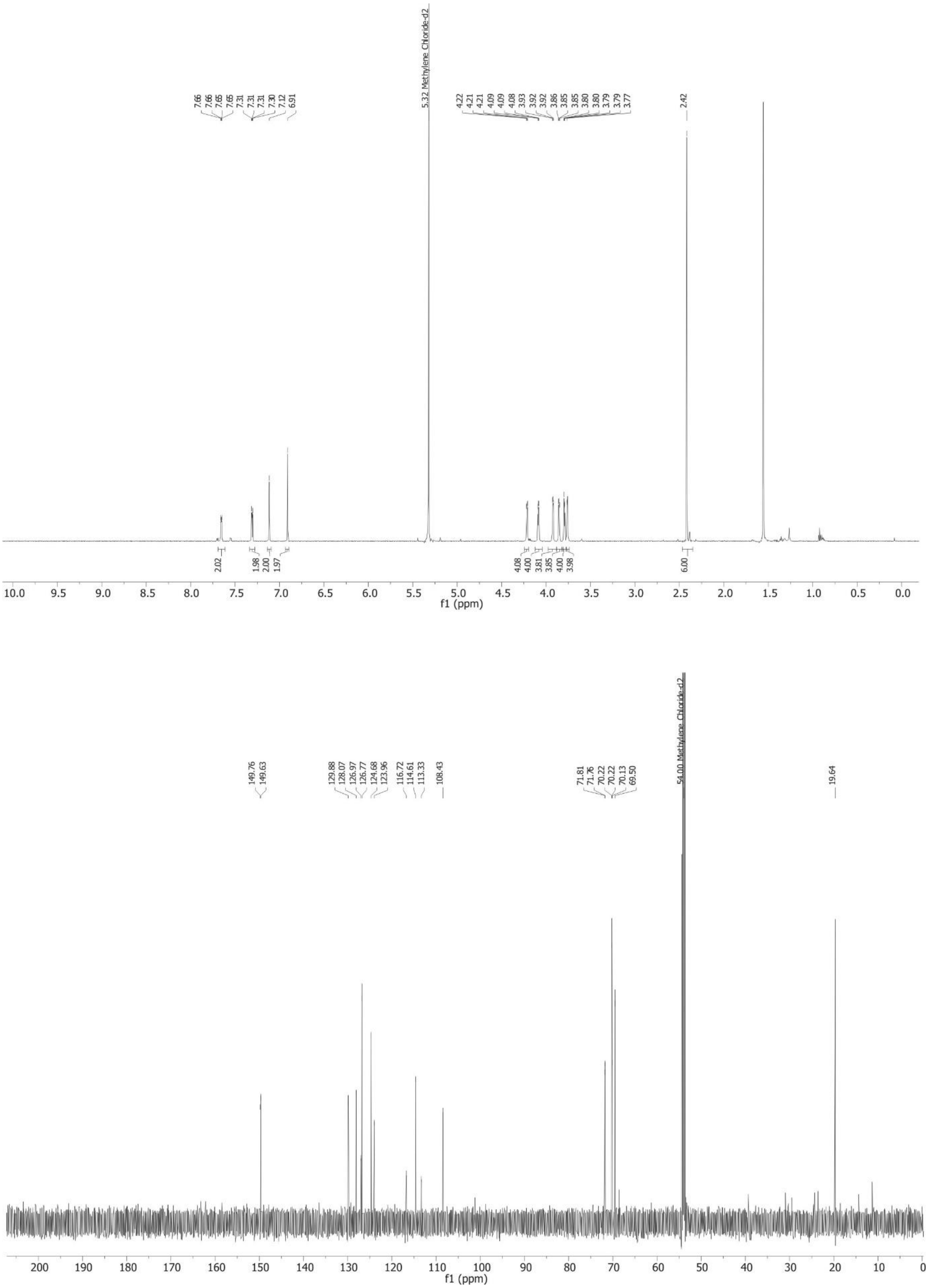

Fig. S22 ^{1}H and ^{13}C NMR spectrum (700/176 MHz, CD_2Cl_2, 298 K) of **exTTFC8**.

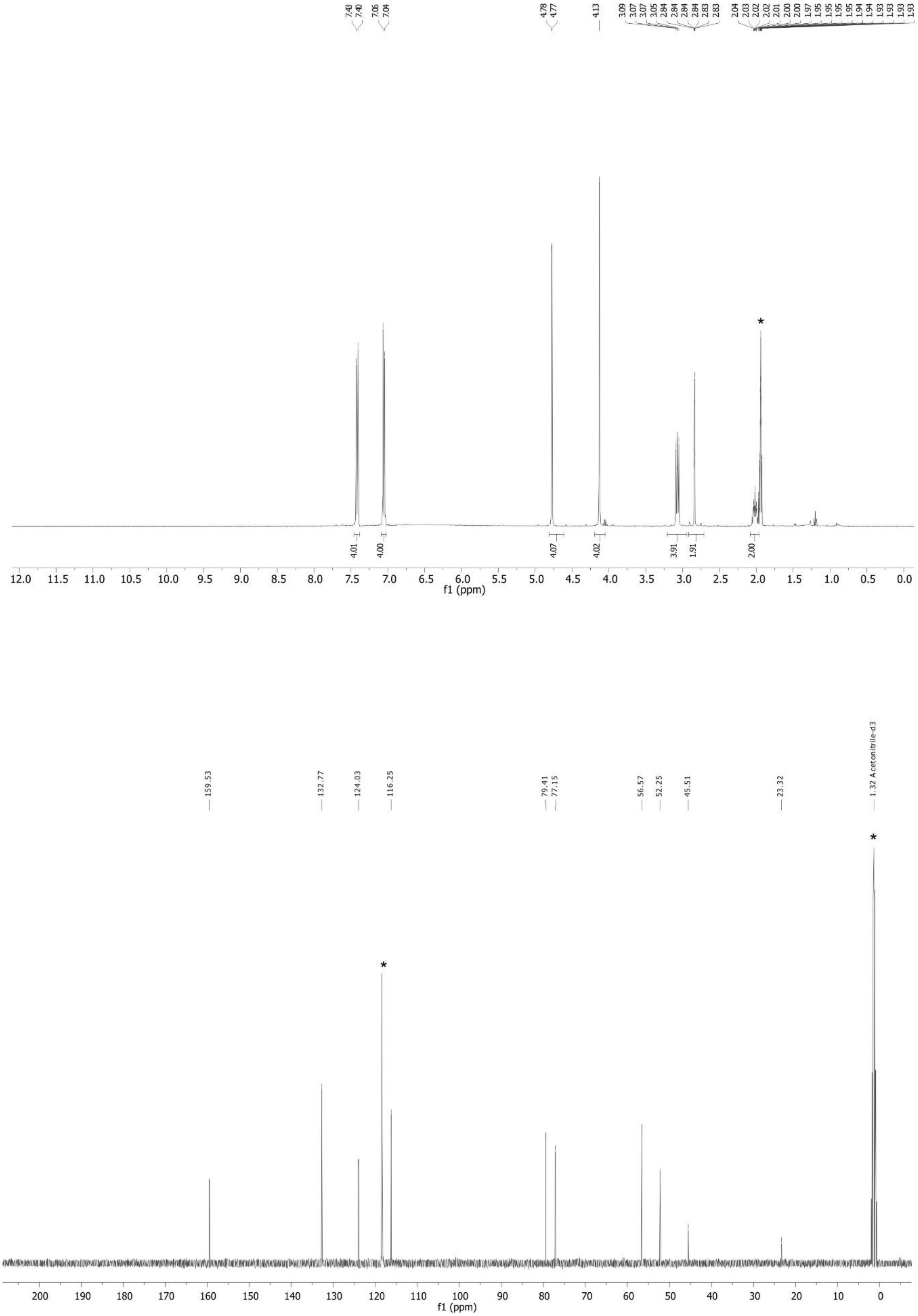

Fig. S23 ^{1}H and ^{13}C NMR spectrum (400/101 MHz, CD_2Cl_2, 298 K) of axle **A2**.

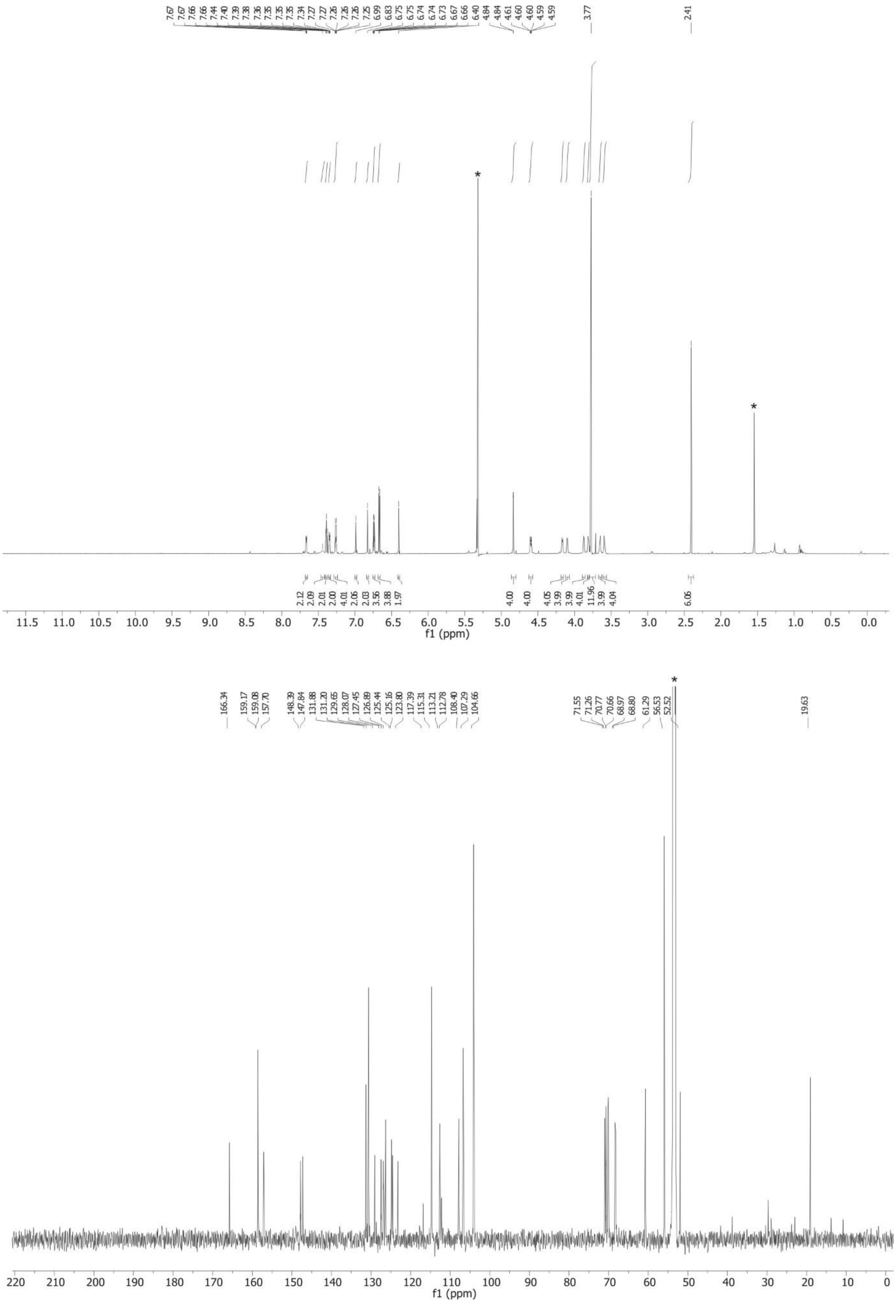

Fig. S24 ^{1}H and ^{13}C NMR spectrum (700/176 MHz, CD_2Cl_2, 298 K) of [2]rotaxane **R1**.

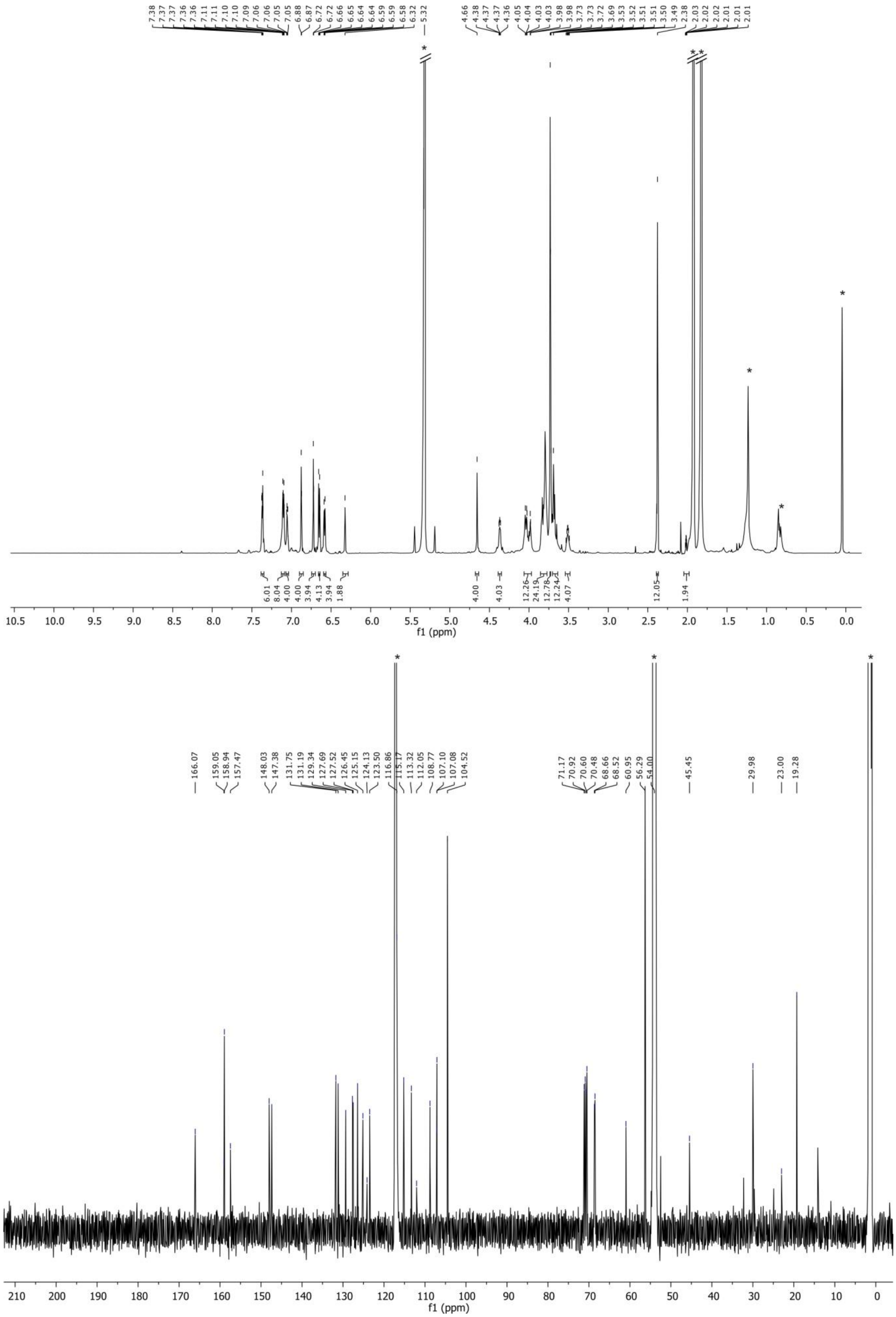

Fig. S25 ^{1}H and ^{13}C NMR spectrum (700/176 MHz, CD_2Cl_2/CD_3CN = 9:1, 298 K) of [3]rotaxane **R2**.

10. Supporting information references

S1 H. V. Schröder, F. Witte, M. Gaedke, S. Sobottka, L. Suntrup, H. Hupatz, A. Valkonen, B. Paulus, K. Rissanen, B. Sarkar and C. A. Schalley, *Org. Biomol. Chem.,* 2018*,* **16***,* 2741.

S2 J. D. Badjic, C. M. Ronconi, J. F. Stoddart, V. Balzani, S. Silvi and A. Credi, *J. Am. Chem. Soc.*, 2006, **128**, 1489.

S3 Z.-J. Zhang, H.-Y. Zhang, H. Wang and Y. Liu, *Angew. Chem. Int. Ed.*, 2011, **50**, 10834.

S4 M. Pal, K. Parasuraman and K. R. Yeleswarapu, *Org. Lett.*, 2003, **5**, 349.

S5 T. Matsumura, F. Ishiwari, Y. Koyama and T. Takata, *Org. Lett.*, 2010, **12**, 3828.

S6 H. V. Schröder, S. Sobottka, M. Nößler, H. Hupatz, M. Gaedke, B. Sarkar and C. A. Schalley, *Chem. Sci.*, 2017, **8**, 6300.

S7 J.-M. Lü, S. V. Rosokha and J. K. Kochi, *J. Am. Chem. Soc.*, 2003, **125**, 12161.

S8 J. R. Aranzaes, M.-C. Daniel, D. Astruc, *Can. J. Chem.*, 2006, **84**, 288.

S9 A. E. Kaifer and M. Gómez-Kaifer, *Supramolecular Electrochemistry*; Wiley, Weinheim, Germany, 1999.

S10 S. Warnke, C. Baldauf, M. T. Bowers, K. Pagel and G. von Helden, *J. Am. Chem. Soc.*, 2014, **136**, 10308.

S11 H. E. Revercomb and E. A. Mason, *Anal. Chem.*, 1975, **47**, 970.

S12 E. A. Mason and E. W. McDaniel, *Transport properties of ions in gases*, Wiley, New York, 1988, 145–159.

S13 G. von Helden, M. T. Hsu, N. Gotts and M. T. Bowers, *J. Phys. Chem.*, 1993, **97**, 8182.

S14 F. Neese, *WIREs Comput. Mol. Sci.*, 2012, **2**, 73.

S15 J. J. P. Stewart, *J. Comput. Chem.*, 1989, **10**, 209.

S16 M. D. Hanwell, D. E. Curtis, D. C. Lonie, T. Vandermeersch, E. Zurek and G. R. Hutchison, *J. Cheminform.*, 2012, **4**, 17.

S17 T. A. Halgren, *J. Comput. Chem.*, 1996, **17**, 490.

S18 TURBOMOLE V7.0 2015, a development of University of Karlsruhe and Forschungszentrum Karlsruhe GmbH, 1989-2007, TURBOMOLE GmbH, since 2007; available from http://www.turbomole.com.

S19 J. Tao, J. P. Perdew, V. N. Staroverov and G. E. Scuseria, *Phys. Rev. Lett.*, 2003, 91.

S20 S. Grimme, J. Antony, S. Ehrlich and H. Krieg, *J. Chem. Phys.*, 2010, **132**, 154104.

S21 S. Grimme, S. Ehrlich and L. Goerigk, *J. Comput. Chem.*, 2011, **32**, 1456.

S22 F. Weigend and R. Ahlrichs, *Phys. Chem. Chem. Phys.*, 2005, **7**, 3297.

S23 K. Eichkorn, O. Treutler, H. Ohm, M. Häser and R. Ahlrichs, *Chem. Phys. Lett.*, 1995, **240**, 283.

S24 F. Weigend, *Phys. Chem. Chem. Phys.*, 2006, **8**, 1057.

S25 M.Sierka, A. Hogekamp and R. Ahlrichs*, J. Chem. Phys.*, 2003, **118**, 9136.

S26 A. Klamt and G. Schüürmann, *J. Chem. Soc. Perkin Trans. 2*, 1993, 799.

S27 J. P. Perdew, M. Ernzerhof and K. Burke, *J. Chem. Phys.*, 1996, **105**, 9982.

S28 R. Sure and S. Grimme, *J. Comput. Chem.*, 2013, **34**, 1672.